

AD-A254 382

AGE

Form Approved

OMB No. 0704-0188

Public reporting burden
gathering and maintain-
collection of information
Davis Highway, Suite 1



Response, including the time for reviewing instructions, searching existing data sources,
information. Send comments regarding this burden estimate or any other aspect of this
quarters Services, Directorate for Information Operations and Reports, 1215 Jefferson
Paperwork Reduction Project (0704-0188), Washington, DC 20503

1. AGENCY USE ONLY (Leave blank)		2. REPORT DATE Summer 1991		3. REPORT TYPE AND DATES COVERED THESIS	
4. TITLE AND SUBTITLE Spatial Resolution Enhancement of SSM/I Microwave Brightness Temperatures and its Impact on Rainfall Retrieval Algorithms				5. FUNDING NUMBERS	
6. AUTHOR(S) Michael R. Farrar, Captain					
7. PERFORMING ORGANIZATION NAME(S) AND ADDRESS(ES) AFIT Student Attending: Florida State University				8. PERFORMING ORGANIZATION REPORT NUMBER AFIT/CI/CIA-92-057	
9. SPONSORING / MONITORING AGENCY NAME(S) AND ADDRESS(ES) AFIT/CI Wright-Patterson AFB OH 45433-6583				10. SPONSORING / MONITORING AGENCY REPORT NUMBER	
11. SUPPLEMENTARY NOTES					
12a. DISTRIBUTION / AVAILABILITY STATEMENT Approved for Public Release IAW 190-1 Distributed Unlimited ERNEST A. HAYGOOD, Captain, USAF Executive Officer				12b. DISTRIBUTION CODE	
13. ABSTRACT (Maximum 200 words)					
92 8 25 055					
14. SUBJECT TERMS				15. NUMBER OF PAGES 72	
				16. PRICE CODE	
17. SECURITY CLASSIFICATION OF REPORT		18. SECURITY CLASSIFICATION OF THIS PAGE		19. SECURITY CLASSIFICATION OF ABSTRACT	
				20. LIMITATION OF ABSTRACT	

THE FLORIDA STATE UNIVERSITY
COLLEGE OF ARTS AND SCIENCES

**SPATIAL RESOLUTION ENHANCEMENT OF
SSM/I MICROWAVE BRIGHTNESS TEMPERATURES
AND ITS IMPACT ON RAINFALL RETRIEVAL ALGORITHMS**

By

MICHAEL R. FARRAR

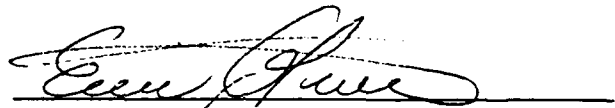
A Thesis submitted to the
Department of Meteorology
in partial fulfillment of the
requirements for the degree of
Master of Science

Degree Awarded:
Summer Semester, 1991

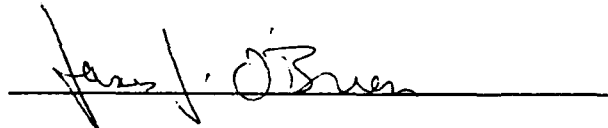
DNC QUANTITY REQUESTED 1

Accession For	
NTIS GRA&I	<input checked="checked" type="checkbox"/>
DTIC TAB	<input type="checkbox"/>
Unannounced	<input type="checkbox"/>
Justification	
By	
Distribution/	
Availability Codes	
Dist	Avail and/or Special
A-1	

The members of the Committee approve the Thesis of Michael R.
Farrar defended on July 25, 1991.

A handwritten signature in cursive script, appearing to read "Eric A. Smith", written over a horizontal line.

Eric A. Smith
Professor Directing Thesis

A handwritten signature in cursive script, appearing to read "James J. O'Brien", written over a horizontal line.

James J. O'Brien
Committee Member

A handwritten signature in cursive script, appearing to read "Peter S. Ray", written over a horizontal line.

Peter S. Ray
Committee Member

Acknowledgements

I wish to thank Chris Kummerow, William Olson, Gene Poe, Richard Savage, Roy Spencer and Jim Hollinger for their generosity and assistance. Their contribution of SSM/I technical information and their valuable time in personal communications was greatly appreciated. I also thank Jim Merritt for his assistance in imaging analysis, as well as his patience in answering all my programming questions.

I would like to express my thanks and gratitude to the members of my committee, James O'Brien and Peter Ray, for their input and suggestions regarding my research. A special thanks goes to my major professor, Eric Smith, for not only giving advise and help when I needed it, but also for allowing me to fail and succeed on my own.

I have saved for last my thanks for those who are the most important: my family. My children, Maynard and Bud, were always excited to see me when I got home and always cheered me up, no matter how bad a day I had. However the most important person was and always will be my wife Tammy. The best part about the whole experience was that she was there to share it with. This is the best part about life too. So Tammy, shut up, I love you!

This research has been supported by NASA Grant NAGW-991. A portion of the computing resources have been provided by the Supercomputer Computations Research Institute at Florida State University under DOE Contract FC058ER250000.

Table of Contents

List of Tables	vi
List of Figures	vii
Abstract	ix
1 Introduction	1
1.1 The deconvolution problem	1
1.2 Motivation for tropical storm rainfall.	4
2 Description of SSM/I Data System	8
2.1 SSM/I instrument	8
2.2 Calibrated brightness temperature data	12
3 The Deconvolution Method	15
3.1 Method of solution	16
3.2 Implementation for SSM/I	22
3.3 Objective specification of tuning parameter	26
4 Validation of deconvolution method	29
4.1 Comparison to linear regression	30
4.2 Self consistency/noise production test	32
4.3 Qualitative geographical assessment of imagery.	33
5 Response of rainfall retrievals to deconvolution	37
5.1 Selection of tropical storm cases	37
5.2 Application to rainfall retrievals	39
6 Summary and Conclusions	55

Appendix: Rainfall retrieval algorithms	59
A.1 Smith and Mugnai (1988)	59
A.2 Spencer et al (1989)	61
A.3 Hinton et al (1991)	63
A.4 Olson (1991)	65
A.5 Kummerow et al (1991)	67
References	69
Biographical Sketch	72

List of Tables

Table Caption	Page
2.1: SSM/I Antenna Beamwidth Characteristics	11
2.2: Spillover and Cross-Polarization Leakage Factors	14
3.1: Average values of γ determined by coastal calibration cases	28
5.1: Tropical storm cases	38
6.1: Percent difference between deconvolved / raw derived rain rates for each tropical storm case at various minimum cutoff rain values	57
6.2: Average percent difference between deconvolved/raw derived rain rates for various minimum cutoff rain values	58

List of Figures

Figure	Caption	Page
1.1	Ground footprint spatial overlap of the four SSM/I frequencies.	2
2.1	SSM/I scan and orbital geometry [from Hollinger <i>et al</i> (1987)]	10
3.1	Geometry for satellite radiometric observations	17
3.2	Raw antenna gain vs. splined average antenna gain	24
4.1	Linear regression geometry and coefficients.	31
4.2	Raw versus deconvolved 19 GHz image of Caribbean basin basin and Florida peninsula.	35
4.3	Raw versus deconvolved 37 GHz image of the western Indian coastline.	35
4.4	Geographical map of western India.	36
5.1	Raw/Deconvolved rain rates for various rainfall algorithms	42
5.2	Raw area-averaged rain rates and percent differences (between deconvolved and raw rain rates) for the algorithm of Smith & Mugnai (1988).	50
5.3	Raw area-averaged rain rates and percent differences (between deconvolved and raw rain rates) for the algorithm of Spencer <i>et al.</i> (1989).	51
5.4	Raw area-averaged rain rates and percent differences (between deconvolved and raw rain rates) for the algorithm of Hinton <i>et al.</i> (1991).	52

5.5	Raw area-averaged rain rates and percent differences (between deconvolved and raw rain rates) for the algorithm of Olson (1991).	53
5.6	Raw area-averaged rain rates and percent differences (between deconvolved and raw rain rates) for the algorithm of Kummerow <i>et al.</i> (1991).	54
A.1	Area integrated rainfall rate as a function of time.	60

Abstract

In this study the impact of spatial resolution enhancement is tested on estimates of typhoon rainfall using microwave measurements from the Special Sensor Microwave/Imager (SSM/I). Passive microwave estimates of rainfall are susceptible to errors from non-complete beam filling. The SSM/I ground footprints for the 19, 22, and 37 GHz channels have considerable overlap and thus deconvolution techniques can be applied to enhance spatial resolution. A Backus-Gilbert matrix transform approach is utilized to accomplish the deconvolution so as to minimize noise amplification as suggested by Stogryn (1978). Various validation procedures are performed to demonstrate the effectiveness of the method.

The deconvolution scheme is evaluated in terms of its impact on integrated rainfall throughout the life cycle of a number of tropical storms which occurred during the 1987 hurricane and typhoon season. This evaluation was performed for a single frequency emission algorithm, a single frequency scattering algorithm, and three multiple frequency algorithms, each with different properties and scientific approaches. While rainfall patterns detected by all algorithms were qualitatively enhanced, quantitative responses were different for each algorithm. The area-averaged rainfall derived from the single frequency emission algorithm was increased by nearly 6%, due to the non-linear relationship of rain rate to brightness temperature, whereas

the rainfall from the single frequency scattering algorithm was decreased by almost 16% due to biases introduced by the deconvolution method. While the multiple frequency algorithms had more complex responses, the difference between deconvolved and raw area-averaged rainfall produced by these methods were less sensitive to deconvolution than the single channel algorithms. The deconvolution method enhanced the quality of the rainfall images produced by all the algorithms, accentuating gradients and other smaller scale features.

CHAPTER 1

Introduction

1.1 The Deconvolution Problem

Due to the very low levels of energy in the microwave regime emanating from the earth-atmosphere system, it has been required that orbiting instruments measure this radiation with large fields of view (FOV) or large "effective" apertures. This feature is necessary to ensure an adequately high signal-to-noise ratio. Since these requirements differ for each SSM/I frequency, this by necessity results in differing ground footprints for each frequency, as illustrated in Figure 1.1. For example, at the 3 dB levels used for the SSM/I instrument, the 19 GHz channel ground footprint is 69 km x 43 km, while the size for 85 GHz is only 15 km x 12 km.

When utilizing measurements at different frequencies in multi-channel retrievals or other objective modeling applications, it is desirable that the measurements be collocated in time and space. Identical antenna boresights for each respective satellite channel (or identical central points of the ground footprints) do not guarantee spatial collocation as channels with larger fields of view sample larger surface areas. For example, a specific SSM/I 19 GHz measurement may sample a small but significant feature such

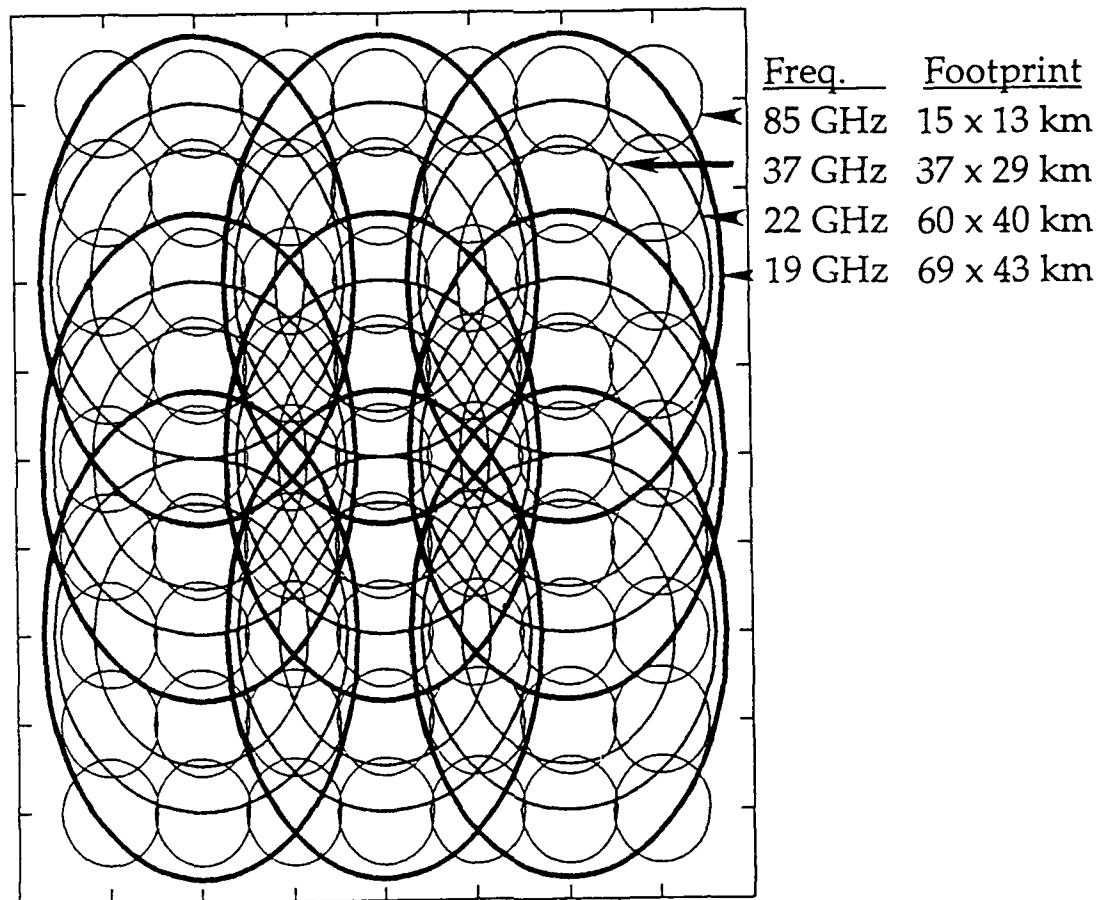


Figure 1.1: Ground footprint spatial overlap of the four SSM/I frequencies.

as a thunderstorm, whereas this feature may effectively lie outside of the FOV of the 85 GHz measurement. Hence comparisons of these measurements at multiple frequencies are hampered by the fact that different phenomena are being sampled by different channels. Therefore, uniform spatial resolution is desired for multi-channel applications.

This requirement poses a dilemma. One must either effectively average the high resolution measurements down to the scale of the low resolution, or alternatively attempt to improve or enhance the low resolution measurements up to that of the high resolution. As the former results in the loss of smaller scale information, the latter is obviously preferred. The optimal methods for increasing spatial resolution rely on an overlap of the gain functions of adjacent antenna measurements. This redundancy of information makes it possible to retrieve information, namely deconvolved brightness temperatures, on scales smaller than those directly sensed by the antenna.

The correction technique presented utilizes a matrix inverse method proposed by Backus and Gilbert (1970) and applied by Stogryn (1978) to the problem of satellite radiometric measurements. Essentially when the density of such measurements is oversampled, the redundancy in the measurements coupled with the antenna gain pattern of the sampling instrument may be combined to produce a set of coefficients, which when applied to measurements surrounding a central point, can produce a data set whose spatial resolution is greater than the original data. Since Backus and Gilbert (1970) showed that such an attempt to enhance resolution leads to an amplification in noise, Stogryn (1978) proposed a method which

simultaneously works to enhance resolution and minimize noise, where these two properties are balanced by a tuning parameter.

Poe (1990) proposed a method by which the low density measurements of the SSM/I lower frequencies were resampled to the higher grid density of 85 GHz. As no attempt was made to increase the spatial resolution of the resampled measurements, the problem of minimizing noise could be neglected. Although this method is quite useful in such applications as imaging, the problem of inequality in spatial sampling between channels is not addressed. This paper seeks a solution to this problem by attempting to increase the spatial resolution and sampling rate of the low resolution SSM/I measurements to that of the high resolution 85 GHz channel. By a careful objective selection of the tuning parameter within Stogryn's theoretical framework, a method is developed which enhances the SSM/I channels to a common resolution, which may prove to be valuable in multispectral applications of satellite data.

1.2 Motivation for tropical storm rainfall

Due to the destruction of flooding associated with hurricanes, the observation and prediction of these tropical storms has long been a high priority. Measurement of rainfall within these storms is important not only for observational reasons, but for forecasting as well. Rodgers and Adler (1981) utilized Nimbus 5 ESMR data to study the precipitation characteristics of several Pacific tropical cyclones. They found that storm intensification was

indicated by an increase in total rainfall, as estimated from the satellite measurements. Also these intensifying storms had an increase in the relative contribution of the heavier rain areas (rain rates $> 5 \text{ mm} \cdot \text{hr}^{-1}$) to the total storm rainfall, and that these maximum rain bands had a smaller radius for intensified storms.

Measurements of rainfall are also valuable in determining storm dissipation. Lewis and Jorgensen (1978) utilized radar data to measure rainfall from Hurricane Gertrude and determined that precipitation intensity decreased rapidly as the storm dissipated. Area integrated rainfall decreased four-fold during a six hour period when the storm was undergoing rapid dissipation. Hence rainfall observations can provide valuable information for intensity forecasting of tropical storms. Due to the unavailability of radar information away from coastlines and the expense of aircraft observations, satellite remote sensing is considered by many to be the best alternative for the monitoring of rainfall within these storms.

Due to the inability of visible and infrared radiation to penetrate the cloud and directly sense the precipitation particles, measurements in the microwave regime have been utilized by a number of current researchers to tackle the rainfall retrieval problem. Wilheit *et al.* (1977) utilized 19 GHz data from the Nimbus 5 Electrically Scanning Microwave Radiometer (ESMR) to retrieve precipitation rates over the ocean. Spencer (1986) and Olson (1989) have also employed data from the Nimbus 7 Scanning Multichannel Microwave Radiometer (SMMR) toward the same goal. One problem which has hampered the results of the studies is the large ground footprints of the

microwave measurements, which leads to non-complete beam filling by precipitating clouds.

Some improvements were made in the latest instrument, the four frequency SSM/I, which has greater ground coverage (~80% increase in swath width) and less noise inherent in its measurements than did its predecessors. However the problem of large ground footprints remains. For reasons explained in the next section, each frequency has different ground footprints, such that each effectively samples a different spatial area. As addressed by Mugnai *et al.* (1990), such mismatches in radiometer fields of view lead to non-linear complications in the radiative transfer models utilized to determine rainfall rates from microwave brightness temperatures. Short and North (1990) compared radar-derived rain rates for convective and mesoscale systems [obtained from shipboard measurements during the Global Atlantic Tropical Experiment (GATE)] with rainfall derived from satellite radiometric measurements made by the Nimbus 5 ESMR. They found that non-complete beam filling of the satellite measurements resulted in a 50% underestimation of rainfall, when compared to the radar-derived values. For these reasons, a deconvolution method is introduced which will attempt to match the differing fields of view of the SSM/I channels, and apply the enhanced measurements to the retrieval of rainfall. As this study is being conducted for tropical storms, which are more likely to contain precipitation regions of greater area coverage and homogeneity than the meteorological systems studied by Short and North (1990), the effects of non-complete beam filling will be less pronounced for this study.

Through the introduction of enhanced measurements, the attempt is made not only to improve the rainfall retrievals, but also the rainfall imagery itself. Since the deconvolution method improves the spatial resolution, boundaries between precipitating and non-precipitating regions which become smoothed by the large instrument fields of view are better revealed. The enhancement of small scale features leads to improvements in the mapping of the precipitation regions of tropical storms, which are useful to tropical storm observation and forecasting as well as to research problems concerned with precipitation retrieval.

CHAPTER 2

Description of SSM/I Data System

The first SSM/I instrument was launched aboard the Defense Meteorological Satellite Program Block 5D-2 Spacecraft F8 on June 19, 1987. The Block 5D-2 spacecraft is in a circular sun-synchronous orbit at an altitude of 833 km with an inclination of 98.8°. This results in an orbital period of 102.0 minutes, yielding 14.1 orbits per day.

2.1 SSM/I instrument

The SSM/I is a series of seven linearly polarized passive microwave radiometers, measuring upwelling radiation at four microwave frequencies. Dual polarization measurements are made at the 19.35, 37.0 and 85.5 GHz window frequencies, while only the vertical polarization at 22.235 GHz water vapor channel is observed. As described in detail by Hollinger *et al* (1987), the radiation is focused to the instrument by an offset parabolic reflector, which is fed by a corrugated, broad-band, seven-port antenna feedhorn. The reflector, feedhorn, radiometers and other subsystems are mounted on a drum unit, which spins with a rotation period of 1.9 seconds. A cold calibration reflector

(a mirror reflecting cold radiation from space) and a hot reference absorber are mounted next to the drum unit, but do not rotate. Once each rotation, the cold reflector and hot reference absorber pass between the feedhorn and the parabolic reflector, such that calibration measurements are taken for each scan.

While the drum containing the feedhorn and radiometers rotate with an axis parallel to the local spacecraft vertical, radiation is sampled aft of the spacecraft track from a nadir angle of 45° . The SSM/I scans left to right (when looking in the aft direction of the satellite track) and actively measures upwelling radiation for 51.2° to either side of the satellite track, resulting in a swath width of 1394 km. During each scan, 128 equally spaced measurements by the 85 GHz channels are made over the 102.4° active scan region. The time interval between these samples is 4.22 msec, so that each measurement along the scan is separated by a ground distance of 12.5 km. This is the same distance which separates each scanline, as the satellite moves 12.5 km along its track during the 1.9 sec rotation.

The other five lower frequency channels make 64 equally spaced measurements every other scan with a sampling interval of 8.44 msec, such that these measurements are separated by 25.0 km along the ground in both the along-track and cross-track directions. A scan line where measurements are made by all channels is denoted as Scan A, while the alternate scan, where only samples by the 85 GHz channels are made, is denoted as Scan B. A pictorial representation of the scan and orbital geometry is presented in Figure 2.1. Also depicted is the instantaneous field of view (IFOV) for each frequency, represented as ellipses which denote the projections of the 3 dB

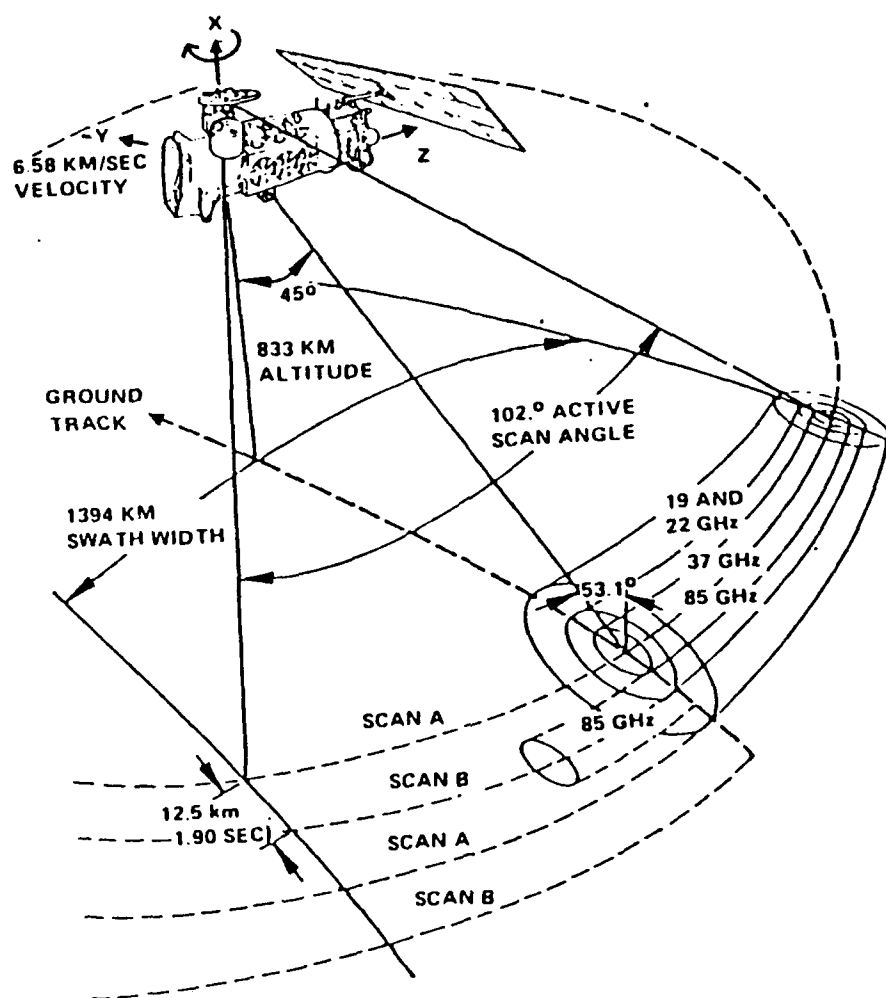


Figure 2.1: SSM/I scan and orbital geometry [from Hollinger *et al* (1987)]

beamwidths on the earth's surface. Since the radiometer filter integrates the instantaneous radiometer output over 3.89 msec for 85 GHz and 7.95 GHz for the other frequencies, an effective field of view (EFOV) is defined which takes into account the finite integration time. While EFOV is significantly larger than the IFOV in the cross-track direction, it is essentially identical in the along-track direction. The IFOV and EFOV beamwidths, as well as their projections on the earth's surface (defined as ground "footprints"), are presented in Table 2.1 for each channel.

Table 2.1: SSM/I Antenna Beamwidth Characteristics

Frequency (GHz)	Polarization	Beamwidth (degrees)			Footprint (km)	
		A.T. IFOV *	C.T. IFOV *	C.T. EFOV *	A.T. *	C.T. *
19.35	vertical	1.86	1.87	1.93	69	43
19.35	horizontal	1.88	1.87	1.93	69	43
22.235	vertical	1.60	1.65	1.83	50	40
37.0	vertical	1.00	1.10	1.27	37	28
37.0	horizontal	1.00	1.10	1.31	37	29
85.5	vertical	0.41	0.43	0.60	15	13
85.5	horizontal	0.42	0.45	0.60	15	13

* - C.T. is Cross Track, A.T. is Along Track

2.2 Calibrated brightness temperature data

Brightness temperature data utilized in this study was obtained from antenna temperature data tapes produced by Remote Sensing Systems. The antenna temperature data set is a compacted version of the Temperature Data Records (TDR's) produced by the Fleet Numerical Oceanographic Center. The data are recorded on 6250 cpi magnetic tapes containing 160 megabytes, where eight such tapes consists of approximately one month of data. For this study, the first 16 tapes produced in this manner were utilized, which included data from July 10 to September 9, 1987.

The conversion of antenna temperatures to brightness temperatures was simultaneously performed with the decoding of the packed antenna temperature data by subroutine DECODE, a software package included with the data tapes provided by Remote Sensing Systems. An antenna temperature is essentially the integration of the viewed brightness temperature field over the gain pattern of the parabolic reflector and antenna feedhorn. Hence this integral must be inverted to obtain a brightness temperature from an antenna temperature.

Wentz (1988) develops an approximation for the brightness temperature (TB) as a function of antenna temperature (TA) and two measured instrument characteristics: feedhorn spillover and cross-polarization leakage. The feedhorn spillover is a measure of the power that enters the feedhorn directly from space, as opposed to the primary source that enters the feedhorn from the antenna. The cross-polarization leakage is a measure of the amount of radiation that enters a port with a polarization orthogonal to that which

the port is attempting to measure. An example would be a measure of the amount of 19 GHz horizontally polarized radiation entering the port of the radiometer measuring 19 GHz vertically polarized radiation. Values of these two properties are reported for each channel in Table 2.2. Polarized brightness temperatures for each of the dual polarized frequencies (19, 37 and 85 GHz) are then calculated by

$$TB_v = A_{vv} TA_v + A_{hv} TA_h + 2.7 A_{ov} \quad (2.1)$$

$$TB_h = A_{hh} TA_h + A_{vh} TA_v + 2.7 A_{oh} \quad (2.2)$$

where the factor 2.7 is the temperature of cold space, and the A coefficients are defined as functions of the spillover (δ) and the cross-polarization leakage χ_p by

$$\begin{aligned} A_{vv} &= (1 + \chi_v) / [(1 - \chi_v \chi_h)(1 - \delta)] \\ A_{hv} &= -\chi_v (1 + \chi_h) / [(1 - \chi_v \chi_h)(1 - \delta)] \\ A_{hh} &= (1 + \chi_h) / [(1 - \chi_v \chi_h)(1 - \delta)] \\ A_{vh} &= -\chi_h (1 + \chi_v) / [(1 - \chi_v \chi_h)(1 - \delta)] \\ A_{vh} &= A_{vh} = -\delta / (1 - \delta) \end{aligned} \quad (2.3)$$

The above equations require both polarizations and therefore may not be applied to the 22 GHz channel, as only the vertical polarization is available. Wentz (1988) utilizes an ocean brightness temperature model to calculate brightness temperatures as a function of antenna temperature for a variety of environmental conditions, yielding the following least-squares linear regression (for 22 GHz):

$$TB_v = 1.01993 TA_v + 1.994 \quad (2.4)$$

Utilizing this set of transformations, the antenna temperature data is then converted to brightness temperatures for use in radiative calculations.

Table 2.2: Spillover and Cross-Polarization Leakage Factors

Frequency (GHz)	Polarization	Spillover (δ)	Leakage (%)
19.35	vertical	0.03199	0.00379
19.35	horizontal	0.03199	0.00525
22.235	vertical	0.02685	0.00983
37.0	vertical	0.01434	0.02136
37.0	horizontal	0.01434	0.02664
85.5	vertical	0.01186	0.01387
85.5	horizontal	0.01186	0.01967

CHAPTER 3

The Deconvolution Method

Various methods have been employed by researchers to describe brightness temperatures of specified regions in terms of measured antenna temperatures. Claassen and Fung (1974) proposed a matrix inverse technique which concentrated on the cross-polarization effects of the measuring instrument. As the measured temperature distributions are approximated by spherical bands, the solution coefficients were determined by integrations of the antenna gain over the spherical bands. A different method was developed by Holmes *et al.* (1975), which was based on Fourier transforms. However these methods have the undesirable side effect of amplifying noise in the measured data. Stogryn (1978) recognized that the problem of inverting a series of antenna temperatures to yield a brightness temperature was mathematically identical to that of inverting antenna temperatures (measured in either the microwave or infrared regime) to yield an atmospheric temperature profile. Research in this field had already shown that attempting to obtain higher resolution in the retrieved profiles could result in the amplification of noise. This trade-off between noise and resolution was recognized by Backus and Gilbert (1970) in their geophysical research. Stogryn's (1978) application of the Backus-Gilbert matrix inverse

method to the problem of estimating brightness temperatures seeks to minimize noise amplification by the use of a tuning parameter. In this research, the technique was implemented in conjunction with SSM/I measurements in such a fashion so as to objectively determine the tuning parameter. A discussion of the method follows.

3.1 Method of Solution

Following Stogryn (1978), consider a satellite-borne radiometer observing the earth-atmosphere system from a known altitude (h) and boresight direction (\hat{s}_0) as illustrated in Figure 3.1. The incremental solid angle viewed by the antenna may be described as:

$$d\Omega = (-\hat{s} \cdot \hat{p} / s^2) dA \quad (3.1)$$

where \hat{p} is the unit vector along a position vector from earth center to the incremental surface area dA , (\hat{s}) is the unit vector from the antenna to area dA , and s is the distance from the antenna to dA . Therefore, the antenna temperature measured along the boresight direction may be expressed as:

$$T_A(\hat{s}_0) = \int_E G(\hat{s}_0, \hat{s}) T_B(\rho, \hat{s}) d\Omega \quad (3.2)$$

where the integral is evaluated over the portion of the earth (E) seen by the satellite.

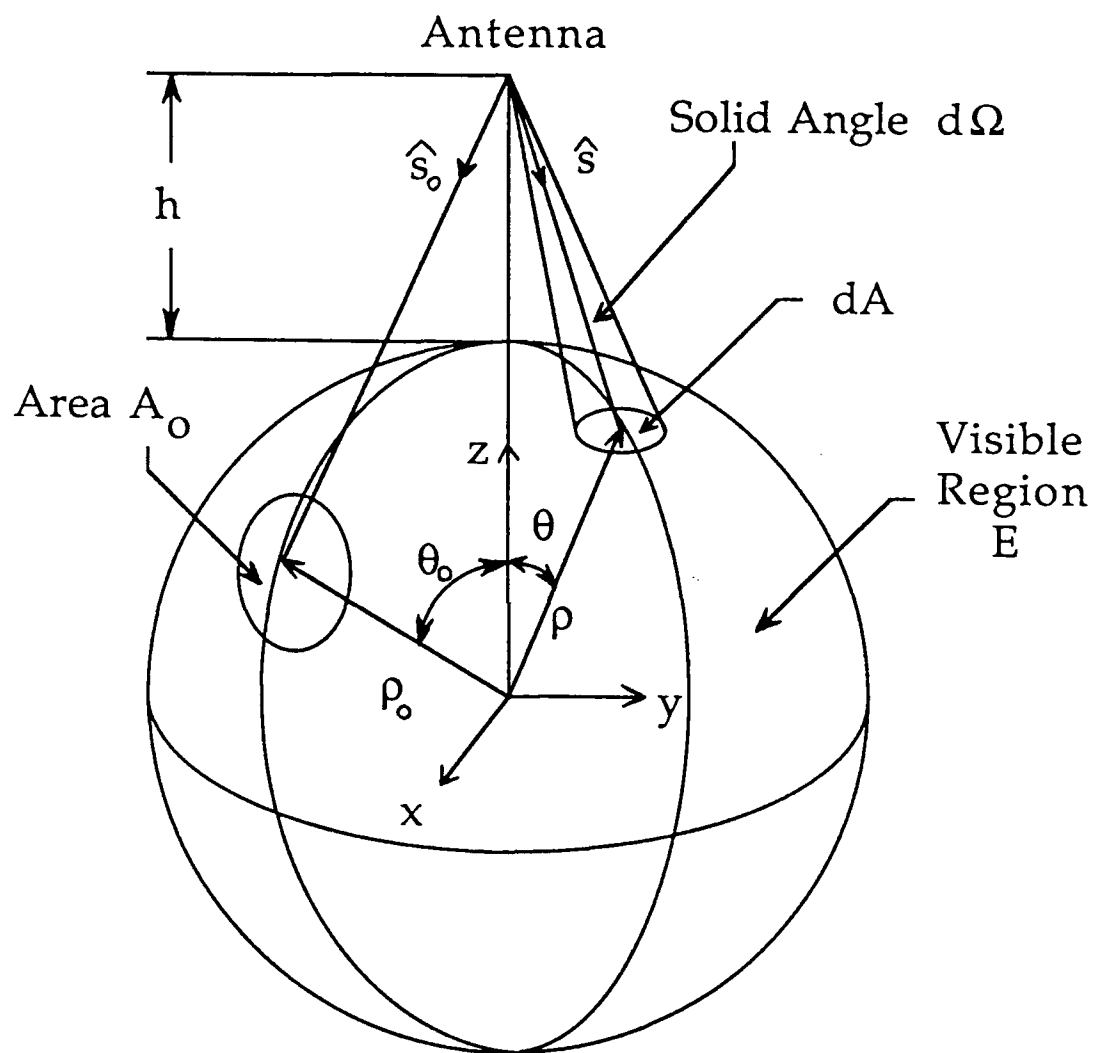


Figure 3.1: Geometry for satellite radiometric observations;
adapted from Stogryn (1978)

In realizing that this process is not instantaneous but is being performed over a finite period of time, two more aspects of the problem arise. Firstly the movement of the instrument as it scans and movement of the platform as it orbits the earth must be considered. This may be dealt with by allowing the appropriate quantities in equation (3.2) to become functions of time. Secondly the integration or measurement time of the instrument itself must be taken into account. This may be accomplished by considering the antenna temperature averaged over the integration time τ . Allowing for these two time dependences leads to:

$$T_A = \frac{1}{\tau} \int_{t_i - \tau/2}^{t_i + \tau/2} \int_E G(\hat{s}_0(t), \hat{s}(t)) T_B(\rho, \hat{s}(t)) (-\hat{s}(t) \cdot \hat{\rho} / s^2(t)) dA dt \quad (3.3)$$

But assuming that the variation in T_B over the integration time τ is negligible, the ith value of a time averaged antenna temperature T_A may be described as:

$$T_{A_i} = \int_E \bar{G}_i(\rho) T_B(\rho) dA \quad (3.4)$$

where the time averaged gain function is:

$$\bar{G}_i(\rho) = \frac{1}{\tau} \int_{t_i - \tau/2}^{t_i + \tau/2} G(\hat{s}_0(t), \hat{s}(t)) (-\hat{s}(t) \cdot \hat{\rho} / s^2(t)) dt \quad (3.5)$$

Consider now that a set of N measurements whose antenna patterns overlap are to be utilized to determine the brightness temperature for some point at ρ_0 on the earth's surface. As this problem is mathematically identical to that considered by Backus and Gilbert (1970), Stogryn (1978) applied their method of solving a system involving a linear combination of the N measurements which approximates $T_B(\rho_0)$:

$$\begin{aligned} T_B(\rho_0) &= \sum_{i=1}^N c_i T_{A_i} \\ &= \int_E \left[\sum_{i=1}^N c_i \bar{G}_i(\rho) \right] T_B(\rho) dA \end{aligned} \quad (3.6)$$

where a substitution for T_{A_i} has been made from equation (3.4). As it is not possible to produce a set of coefficients c_i which yield a perfect solution for $T_B(\rho_0)$, the problem is reduced to finding a set coefficients which most closely produces the resultant brightness temperature.

By considering an integral of the form:

$$Q_R = \int \left[\sum_{i=1}^N c_i \bar{G}_i - F(\rho, \rho_0) \right]^2 J(\rho, \rho_0) dA \quad (3.7)$$

and a normalization constraint:

$$\int \sum_{i=1}^N c_i \bar{G}_i dA = 1 \quad (3.8)$$

then by appropriate choice of F and J , Q_R can be minimized. The F and J functions are chosen according to a particular application. J is a weighting function which allows emphasis to be placed on desired regions in the integration but can be set to unity if this dependence is not relevant. If F is chosen to be equal to a constant value of $1/A_0$ within the area A_0 and equal to zero outside this area, the minimization of equation (3.7) will yield the best estimate of the average brightness temperature over the specified area A_0 .

Another aspect affecting the procedure is the propagation of instrument noise into the desired solution of the brightness temperature. As the variance of this random noise is equal to $(\Delta T_{rms})^2$, the variance in the resultant solution of the brightness temperature is:

$$Q_N = \vec{c}^T E \vec{c} \quad (3.9)$$

where \vec{c} is the vector with elements c_i and E is the error covariance matrix. As the noise in this case is purely random and hence no correlation exists between successive measurements, E is a diagonal matrix whose diagonal elements are $(\Delta T_{rms})^2$. In order to ensure a minimum propagation of noise to the solution, equation (3.9) could be minimized with the normalization constraint of equation (3.8).

The method utilized in this research attempts to balance the trade-off of resolution and noise, with the constraint of equation (3.8), by minimizing the combination of Q_R and Q_N , i.e.:

$$Q = Q_R \cos \gamma + w Q_N \sin \gamma \quad (3.10)$$

where w is chosen to insure that Q_R and Q_N are dimensionally consistent and the tuning parameter γ allows emphasis to be placed on resolution or noise as it is varied from 0 to $\pi/2$, respectively.

The solution to the minimization may now be expressed. Allow G to be the $N \times N$ matrix with elements:

$$G_{ij} = \int \bar{G}_i(\rho) \bar{G}_j(\rho) dA \quad (3.11)$$

Then the solution vector \vec{c} becomes:

$$\vec{c} = Z^{-1} \left[\cos \gamma \vec{v} + \frac{(1 - \cos \gamma) \vec{u}^T Z^{-1} \vec{v}}{\vec{u}^T Z^{-1} \vec{u}} \right] \quad (3.12)$$

where:

$$\vec{u}_i = \int \bar{G}_i(\rho) dA \quad (3.13)$$

$$\vec{v}_i = \int \bar{G}_i(\rho) (1/A_0) dA \quad (3.14)$$

$$Z = \cos \gamma G + w \sin \gamma E \quad (3.15)$$

The solution of equation (3.12) in conjunction with equation (3.6) and the specification of G yields the solution for $T_B(\rho_0)$.

3.2 Implementation for SSM/I

Once the deconvolution method has been developed, several specific characteristics of the measuring instrument and scan geometry must be incorporated to uniquely specify the problem. One aspect is the number of neighboring measurements that can be used in the inversion. As the SSM/I employs a conical scanner, which causes the orientation of neighboring footprints to be different for each position along a scan line, the choice of a constant number of footprints for all scan positions is undesirable. The criterion thus chosen was one of proximity, such that all footprints whose center points lie within a specified elevation from the boresight would be considered. An elevation cutoff value of 1.5° is selected in attempt to balance a trade-off. The gain at this elevation drops by approximately an order of magnitude for 19 GHz (by two orders of magnitude for 37 GHz), while the gains at smaller elevations would still have relatively large values and significant contributions to the measured brightness temperature might be neglected. Conversely, larger values of the elevation cutoff would involve many more measurements and hence slow the calculation process.

Aside from orbital and scanning characteristics, two instrument specifications are needed to implement this method: instrument noise levels and antenna gain patterns for each channel. The error covariance matrix \mathbf{E} may now be defined as previously described by assigning to ΔT_{rms} the appropriate values for each channel, as described by Hollinger (1987).

As only limited gain information was recorded for the instrument utilized (instrument S/N 002 aboard DMSP F8), some interpolation is

necessary for the \bar{G} function. The gain function is determined at a resolution of $.1^\circ$ in elevation angle (displacement from boresight), but only at intervals of 45° in azimuth. In an attempt to produce spatially complete patterns, the gain data are interpolated to a resolution of $.01^\circ$ in elevation angle by a cubic spline. Due to the azimuthal symmetry of the patterns, it was found feasible to average over azimuth, yielding gain patterns which are functions of elevation angle only. Figure 3.2 depicts the interpolated gain versus the eight azimuthal cuts for the 37 GHz and 19 GHz channels. The azimuthally averaged gain matches the gain for each azimuthal cut quite well for elevations less than 1.5° , the cutoff value utilized.

The contribution of brightness temperatures away from the boresight to the measurement of the brightness temperature along the boresight is accomplished by taking advantage of the overlapping antenna patterns of neighboring measurements. Hence the gain of each measurement with respect to the relative position of its neighbors must be determined. This in turn requires a knowledge of the scan geometry in order to describe the relative positions between successive measurements and their ground footprints. As the SSM/I employs a conical scanner, the exact determination of such a geometry leads to computational complexity. However, by making a tangent plane approximation, oriented such that this plane is tangent to the earth's sphere at the point of intersection of the boresight and the earth's surface, it is possible to obtain nearly exact results for small displacements away from the boresight. After the displacement of neighboring footprints from the boresight is found in terms of elevation and azimuth, they are matched with the interpolated antenna patterns to yield the appropriate gain

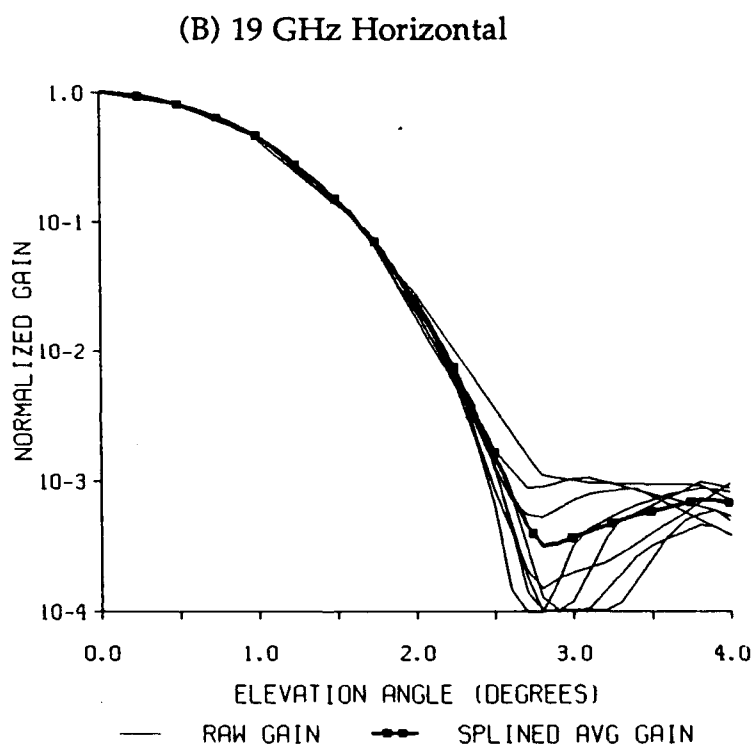
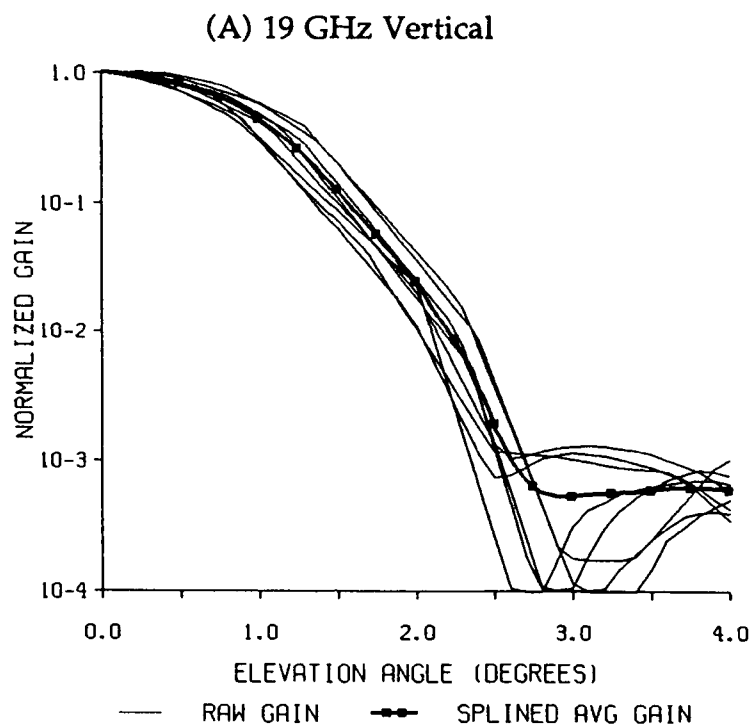


Figure 3.2: Raw antenna gain vs. splined average antenna gain

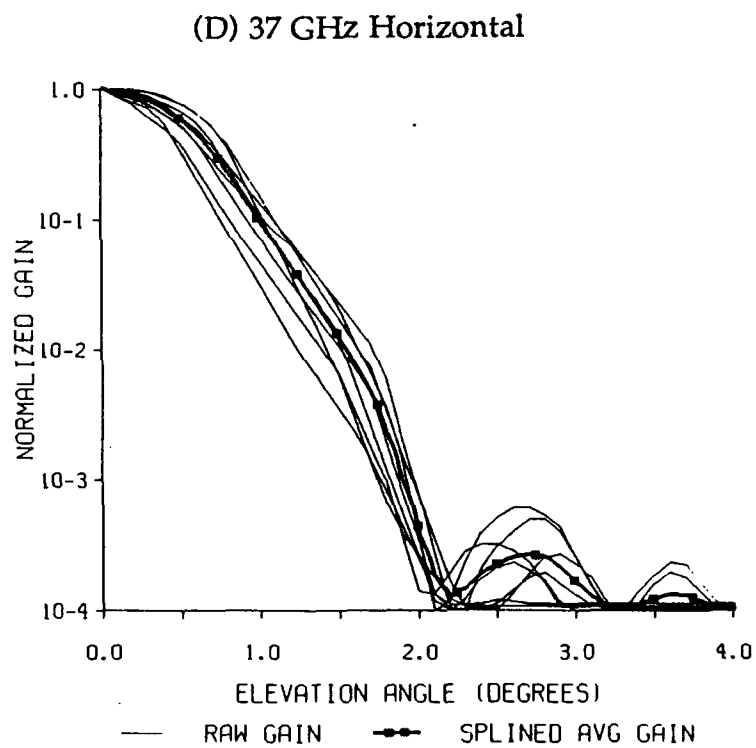
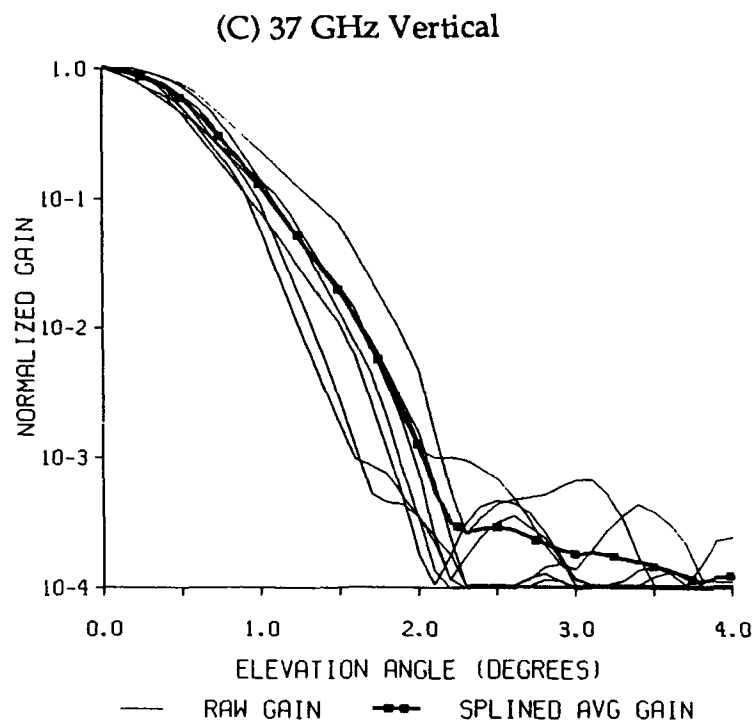


Figure 3.2: Continued

values. Once the instrument gain is properly incorporated, the G matrix may be uniquely specified allowing the solution vector c to be obtained.

3.3 Objective specification of tuning parameter

One final parameter remains unaccounted for in the solution vector: the tuning parameter γ , which attempts to balance the trade-off between resolution and noise. Since there is no apriori rule which uniquely determines this parameter, γ is chosen on the basis that the inter-correlation between the deconvolved channel and the next highest frequency channel is maximized. A number of test data cases have been analyzed in this fashion to select a set of optimum tuning parameters. In the process, the selection of test cases which may lead to negative correlations has been avoided, such as precipitation. The scattering effects of precipitation-sized particles at the higher frequencies (i.e., 85 GHz) can lead to radiation losses and hence minimum values in the brightness temperatures. However these same precipitation regions will have little scattering effect at the lower frequencies, and due to emission effects, will in fact appear as relative maxima. This negative correlation due to precipitation, when coupled with the remainder of the scene which is positively correlated, contaminates the cross-channel correlation approach in determining optimal tuning parameters.

Another consideration is that there must be sufficiently high brightness temperature gradient information such that the blurring effect of the lower resolution channels is measurable. Such gradients are found along coastlines,

where cool ocean brightness temperatures transition rapidly to warm land brightness temperatures. Hence, rain-free coastline cases were chosen to determine the γ 's with the cross-correlation technique. Approximately one hundred coastline cases were selected from four ocean basins: Western Pacific, Eastern Pacific, Caribbean, and Indian Ocean coastlines.

After determining the optimum γ at each channel for all the selected coastline cases, the results were averaged to yield a set of coefficients (given in Table 3.1) which could be utilized for general applications. Such applications may include those which require computational speed, as the implementation of such predetermined coefficients avoids the extra computer time required to calculate the optimum values. Another such application is made where the cross-channel correlation technique is not applicable, such as for precipitation cases.

Of note is that the solutions are dependent on the choice of γ , and that utilization of average γ 's does not always yield the level of detail which can be obtained by the case sensitive approach. Hence there may be no universal best set of γ 's, although the search is still ongoing. For the purposes of validation discussed in the next chapter, only applications where the tuning parameter has been determined independently on a case by case basis were used.

TABLE 3.1: Average values of γ determined by coastal calibration cases

Channel	Polarization	Tuning Parameter (γ)
37 GHz	vertical	$0.53 \pi/2$
37 GHz	horizontal	$0.48 \pi/2$
22 GHz	vertical	$0.13 \pi/2$
19 GHz	vertical	$0.13 \pi/2$
19 GHz	horizontal	$0.08 \pi/2$

CHAPTER 4

Validation of Deconvolution Method

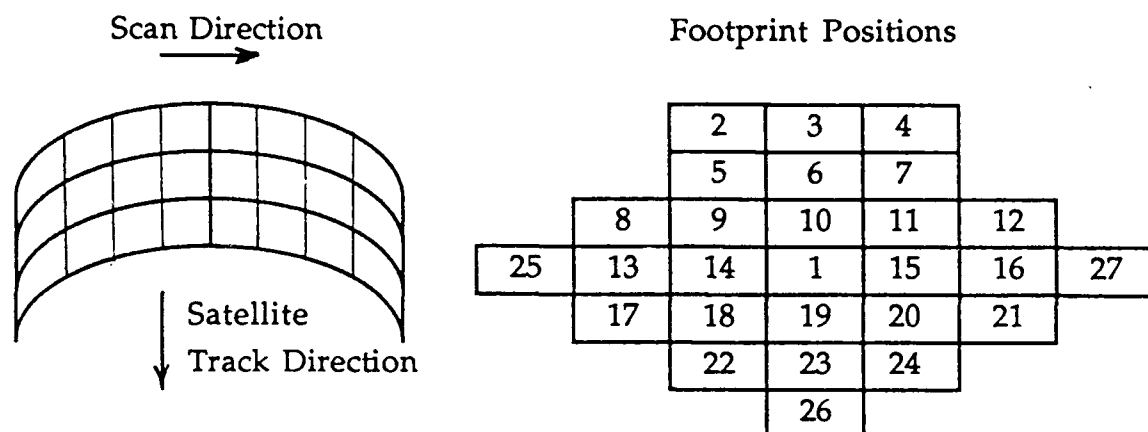
The only way to *truly* validate the resolution enhancement of the SSM/I low frequency channels would be to compare enhanced measurements to those actually made at the desired high resolution. However, as such high resolution measurements of the SSM/I low frequency channels coincident to their actual low resolution measurements do not exist, such comparisons cannot be made and hence other methods of validation must be pursued.

Three forms of validation were selected to illustrate the effectiveness of the deconvolution method. First a simple linear regression technique is presented as a standard by which the deconvolution method may be compared. Secondly, a self consistency test was performed by averaging a high resolution data set to a lower resolution, whereby the deconvolution procedure is invoked on the averaged set in an attempt to retrieve the original high resolution data. Thirdly, a qualitative comparison of deconvolved and raw imagery was performed to determine the visual improvement made by the method in terms of its enhancement of actual geographic features.

4.1 Comparison to linear regression

The first way of demonstrating the effectiveness of such a rigorous procedure as the deconvolution method is to show that it can improve on the results of a simpler technique. A linear regression procedure developed by Spencer (1991) provides the method of comparison. A linear regression was performed on a set of horizontally polarized 19 GHz brightness temperatures along coastlines to produce a set of regression coefficients, which when applied to the raw 19 GHz brightness temperatures, produced a new set of brightness temperatures which most closely matched the horizontally polarized 37 GHz brightness temperature pattern. The coefficients and the geometry for their application are presented in Figure 4.1.

As this linear regression method represents the equivalent of an enhancement of 19 GHz brightness temperatures to the resolution of 37 GHz, the deconvolution method was reconfigured to this enhancement resolution for the purpose of comparison. When applied to the 19 GHz brightness temperatures for several cases, the linear regression of Spencer (1991) explains 97.95% of the total variance in the 37 GHz data, whereas the deconvolution method explains 98.65% of the variance. This represents a 34.15% quantitative improvement in terms of reducing the unexplained variance. However, even though the deconvolution method leads to an improvement over the linear regression technique, the raw 19 GHz data themselves explained such a high percentage of the variance (over 97%) that such a comparison by itself is not an adequate proof of the superiority of the method.



Footprint	Scan Location						
	4-11	12-19	20-27	28-37	38-45	46-53	54-61
1	2.501	2.209	2.199	2.109	2.070	2.551	2.428
2	0.081	-0.001	-0.025	-0.069	-0.135	-0.082	-0.018
3	0.028	0.097	0.224	0.237	0.224	0.049	0.031
4	0.004	-0.079	-0.132	-0.023	0.047	0.136	-0.031
5	-0.446	-0.199	0.094	0.204	0.369	0.212	-0.001
6	0.041	-0.213	-0.720	-0.729	-0.795	-0.344	0.107
7	-0.061	0.145	0.353	0.106	0.024	-0.287	-0.289
8	-0.035	0.018	0.126	0.092	-0.020	-0.020	0.015
9	0.117	0.002	-0.311	-0.348	-0.240	0.054	-0.087
10	-0.001	0.161	0.453	0.505	0.568	0.090	0.169
11	0.007	-0.127	-0.200	-0.262	-0.327	-0.044	-0.064
12	0.0	0.073	0.0	0.047	0.035	0.076	0.107
13	0.200	0.141	-0.010	0.051	0.080	0.023	0.219
14	-0.614	-0.488	-0.361	-0.248	-0.312	-0.500	-0.753
15	-0.554	-0.382	-0.394	-0.317	-0.286	-0.670	-0.666
16	0.183	0.018	0.032	0.169	0.178	0.168	0.122
17	-0.028	-0.004	0.086	0.096	0.120	0.186	0.105
18	0.045	0.024	0.107	-0.131	-0.280	-0.346	-0.100
19	-0.128	-0.053	-0.291	-0.163	-0.002	-0.130	0.0
20	-0.055	-0.239	-0.144	-0.116	0.0	0.231	-0.021
21	0.0	0.145	0.152	0.0	-0.045	-0.048	0.0
22	-0.123	0.015	-0.069	0.0	0.0	-0.072	-0.300
23	0.136	-0.128	-0.102	-0.275	-0.364	-0.231	0.139
24	-0.348	-0.109	-0.054	0.040	0.0	-0.074	0.0
25	0.083	0.060	0.075	0.127	0.169	0.147	0.0
26	-0.033	-0.036	-0.047	-0.054	-0.032	-0.034	-0.074
27	0.0	-0.050	-0.041	-0.048	-0.046	-0.041	-0.038

Figure 4.1: Linear regression geometry and coefficients. Actual scan geometry is illustrated at top left. Coefficients, given at the bottom, are multiplied by brightness temperatures around a central point (designated as footprint location #1 by geometry at top right)

4.2 Self-consistency / noise production test

A self-consistency test was chosen as a second quantitative means of validation. If the high resolution measurements are smoothed to a lower resolution, a proper enhancement procedure performed on the smoothed data should yield an enhanced data set very close to the original high resolution data. This self-consistency approach was performed on several sets of 85 GHz vertically polarized brightness temperatures to numerically validate the deconvolution method. The 85 GHz data were subjected to the same deconvolution procedure as previously described, with two exceptions. Whereas as before the resolution of the low frequency channels had been increased utilizing their respective gain functions, here the resolution has been reduced to that of 37 GHz utilizing the gain function of the 85 GHz instrument. Secondly, as the act of smoothing inherently reduces noise, the consideration of noise reduction in the procedure can be neglected by choosing a zero value for the tuning parameter ($\gamma = 0$).

The smoothed data set was then enhanced back to the 85 GHz resolution (by the deconvolution method as originally described), where it was compared with the original data in terms of an rms difference. For a perfect enhancement with no noise production, such a comparison should result in an rms difference between the original data and the smoothed/re-enhanced data of no more than the inherent instrument noise. The average rms difference for the series of 85 GHz vertically polarized test cases was 1.47 K, roughly twice the value of 0.75 K reported by Hollinger (1987) as the noise

inherent in the 85 GHz instrument. Hence the enhancement process only generates approximately 0.75 K of added noise.

Note that the smoothing and enhancement processes differ in their choices of gain functions, limits of spatial integration, and selection of tuning parameters. Thus their implementations are independent and are not merely an inversion of one another. Hence this validation approach is not simply a measure of how well the matrix processes can be inverted but is instead a legitimate estimate of the effectiveness of the enhancement procedure.

4.3 Qualitative assessment of imagery

If the procedure is *truly* improving the spatial resolution of the measurements, prominent geographical features should be enhanced in the resultant images. Thus a qualitative validation procedure has been applied for a number of geographical cases to reinforce the conclusions of the previous section. Such a case for the Caribbean basin and Florida peninsula is presented in Figure 4.2, where (A) a raw 19 GHz image and (B) an enhanced image are presented for comparison. Whereas the actual raw measurements blur the boundary between land and ocean and hence underestimate the brightness temperatures of the land along the coast, the deconvolved data not only enhances the resolution but tightens this coastal brightness temperature gradient. This blurring effect is especially noticeable in many Caribbean islands, where due to their small size, the brightness temperatures are smeared not only along the coastlines but throughout the interiors as well.

The deconvolution procedure improves on the coastlines and actually increases the brightness temperature values of the relatively warmer and drier island interiors, most dramatically illustrated in the depiction of Cuba, Andros, Jamaica, and Hispaniola. The process also works in the other direction so as to enhance a relative minimum, as illustrated by Lake Okeechobee (in south Florida). Whereas the raw image of the lake is blurred with the surrounding warmer land, the deconvolved image enhances the boundaries while producing a lower brightness temperature for the relatively colder lake waters.

Another such case for the western coast of India is illustrated in Figure 4.3. As for the Caribbean case, the deconvolution procedure better defines the coastal brightness temperature gradient. When compared to a geographical map as illustrated in Figure 4.4, the deconvolution procedure enhances the Indian coastline to a resolution which better matches the actual geographic features. What is most notable is the improvement of the actual geographic coastline, depicted by the enhanced definition of the Gulfs of Kutch and Khambhat along with the peninsula of Gujarat that lies between. Whereas this peninsula is blurred by the raw image, the deconvolved image actually matches the geographic pattern, highlighted by the shape of the tip of the peninsula, near the city of Okha (located by * in Figure 4.4). In addition to the two examples shown, many more cases were examined to determine the effectiveness of the method in improving the geographic details of the scenes. The deconvolution method was found to consistently tighten the coastal brightness temperature gradients, bring out small features blurred by the raw data, and better depict actual geographic features found in the examined cases.

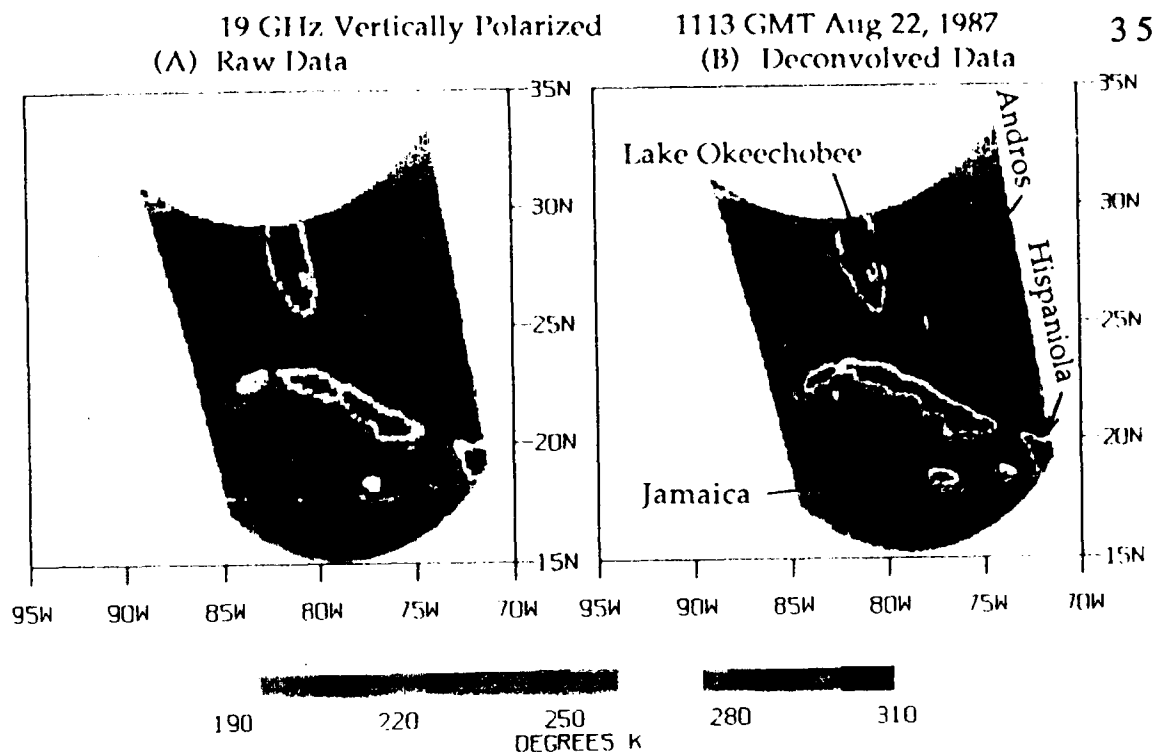


Figure 4.2: Raw vs. deconvolved 19 GHz image of Caribbean basin and Florida.

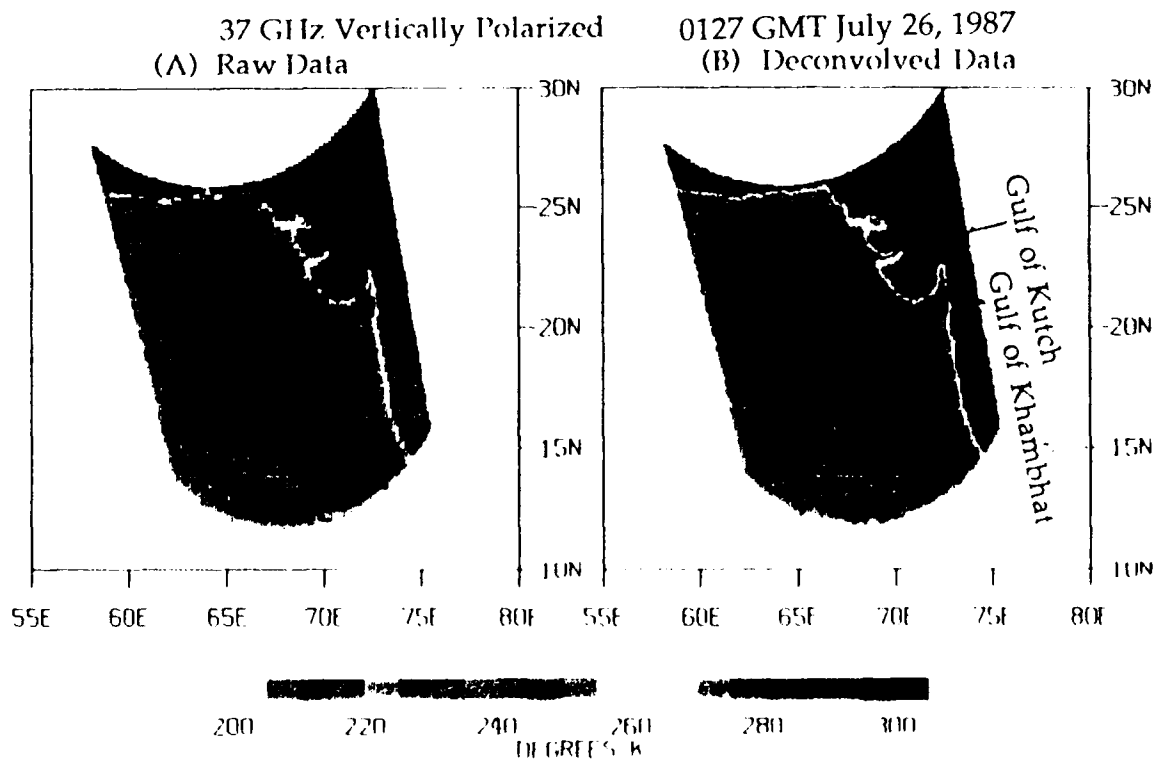


Figure 4.3: Raw vs. deconvolved 37 GHz image of the west Indian coastline.



Fig. 4.4: Geographical map of western India. The city of Okha at the tip of Gujarat is indicated by an asterisk(*).

CHAPTER 5

Response of Rainfall Retrievals to Deconvolution

5.1 Selection of tropical storm cases

The data set utilized consists of three full months of worldwide SSM/I brightness temperature measurements, from July 10 to September 9, 1987. The selection of cases was performed by a systematic search of the data for SSM/I overpasses of each recorded tropical storm. This search was aided by the time/location history documented for each prevalent tropical storm region. Hoffman *et al.* (1987) provided the information for the eastern hemisphere cyclones, while those for the western hemisphere were produced by Case and Gerrish (1988) for the Atlantic and Cross (1988) for the eastern Pacific. Such records greatly simplified the search for good tropical storm cases, as it was known exactly when and where to look.

The only remaining problem was due to the nature of the polar orbiting spacecraft. As the sun-synchronous satellite passed over the same spot only once every twelve hours, and the width of its scan swath was only 1394 km, many such overpasses sampled only a portion of the tropical storm or missed it altogether. Although this was present throughout the life of each tropical storm, the degree of the problem varied. For some cases, many consecutive

overpasses viewed a storm well, only to miss the next several in a row. Other cases viewed a storm for nearly all overpasses, but only partially, as it consistently missed the eye. Still other cases viewed the majority a storms life cycle, only to miss the crucial time when the storm was at or near its maximum strength. In selecting the cases studies, all of these considerations were taken into account. Cases which had inadequate coverage during a particular time period of the storm, cases which had many consecutive missed overpasses, and cases which consistently sampled only the periphery of the storm while missing the eyewall were not used. The remainder of the cases which passed these screening tests were then deemed adequate to represent the life cycle of each storm. For these cases (listed in Table 5.1), a fairly complete temporal study of precipitation could be accomplished.

Table 5.1: Tropical storm cases

Name	Status	Region	# Overpasses
Arlene	hurricane	Atlantic	8
Betty	super typhoon	West Pacific	9
Cary	typhoon	West Pacific	10
Greg	hurricane	East Pacific	5
Hillary	hurricane	East Pacific	9
Thelma	super typhoon	West Pacific	7
Wynne	typhoon	West Pacific	10

5.2 Application to rainfall retrievals

The quantitative effect of the deconvolution procedure on the actual brightness temperatures was evaluated in terms of its impact on five microwave rainfall retrieval algorithms, applied to the tropical storm cases discussed in the previous section. Three of the algorithms utilized involved only 19 GHz and/or 37 GHz brightness temperature data. The first of these is the single channel emission-based algorithm for unpolarized 19 GHz measurements, developed by Smith and Mugnai (1988). The second algorithm examined is the scattering-based algorithm of Spencer *et al.* (1989), which utilizes polarization differences at 37 GHz to measure the scattering effects of precipitation in terms of a polarization corrected (brightness) temperature (PCT), from which rainfall rates were then inferred. The third rainfall algorithm is that of Hinton *et al.* (1991), a hybrid physical model/statistical regression developed for the Nimbus 7 SMMR instrument. It is actually a weighted average of four single channel algorithms, (developed for 18H, 18V, 37H and 37V GHz) where the weights are determined from the response of each channel to the magnitude of the detected rainfall. Of note is that while the regression equations were developed for the SMMR frequencies of 18 and 37 GHz, they were used with SSM/I data measured at 19 and 37 GHz. Hence the results for this algorithm are presented in terms of the effects of the deconvolution procedure alone, and are not to be interpreted as an evaluation of the rainfall retrieval itself when SSM/I data is employed.

The other two algorithms employed in this study involved all four SSM/I frequencies. The first of these is the method of Olson (1991), a

statistical regression of transformed brightness temperature parameters (derived from all SSM/I frequencies) to radar-retrieved rainfall data. The second is that of Kummerow *et al.* (1991), which utilizes the inversion of hydrometeor profile relationships to retrieve rainfall rates. As both of these algorithms are currently under development and are not yet fully complete, any remarks made concerning their performance are to be considered as preliminary. A more detailed discussion of all five algorithms is presented in the Appendix.

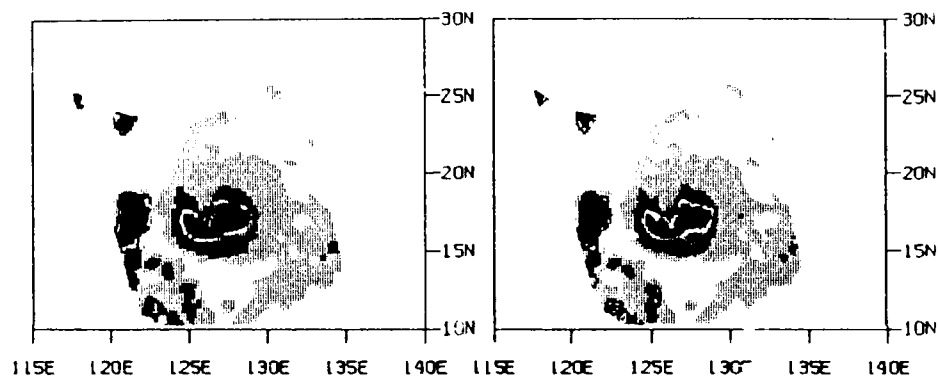
Initially, the deconvolution procedure was applied to the SSM/I measurements, yielding a set of both raw and deconvolved brightness temperatures. Then both sets were introduced to each of the five rainfall algorithms to produce five sets of raw and deconvolved rainfall rate maps. This process was performed for all overpasses for each of the tropical storm cases listed in Table 5.1.

When algorithms devised for retrievals over ocean backgrounds are utilized for scenes which include land, the emission from these land sources can appear as rainfall regions. As an example, Figure 5.1a illustrates the contamination of the Phillipine islands in the rain field of Super Typhoon Thelma depicted by the algorithm of Smith and Mugnai (1988). As the relatively warm land surfaces have not been filtered out but instead appear as heavy rain areas, a calculation of an area-averaged rainfall rate over the scene will be distorted by the contribution from the land. Although many methods exist which screen out the data over land sources, it is important to utilize the same screening method for all retrieval algorithms to insure consistency in their comparisons. In this study the land areas were removed by only

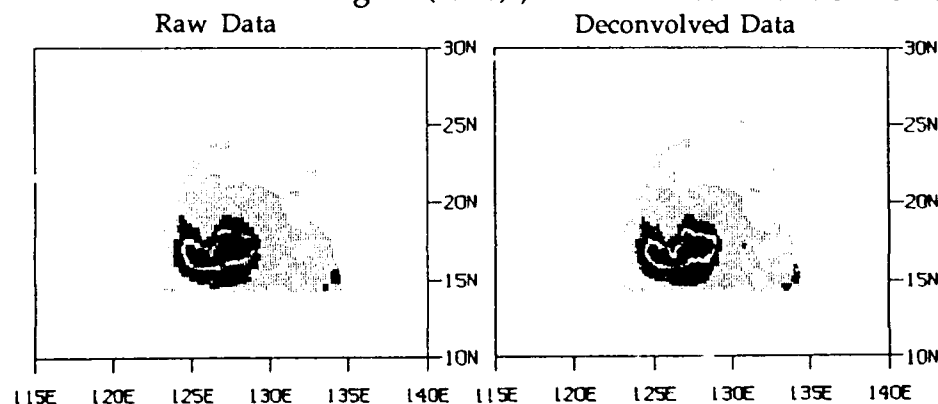
considering measurements made within a specified box, where no land was included. A depiction of the rain field from Figure 5.1a without the land is shown below it in Figure 5.1b. Rainfall maps of the same scene derived from the other four rainfall algorithms are presented in Figure 5.1c-f. Qualitative examination of each of these images reveals one positive effect of the deconvolution method. Smaller rainfall areas such as the bands of the depicted typhoon are enhanced in their definition, as well as the tightening of the gradients between precipitating and non-precipitating areas. Such improvements in the definition of the images were observed for terrestrial geographic features in Chapter 4.

A more quantitative evaluation of the effect of the deconvolution method on the rainfall retrieval algorithms is its impact on area-averaged rainfall. After the rainfall maps were made for each overpass of each selected storm case, they were integrated over area to yield an area-averaged rainfall rate over the scene. The result of this process gives an account by each rainfall algorithm of the area-averaged precipitation history for each storm. As was evident from the rainfall maps, the methods of Hinton *et al.* (1991) and Olson (1991) produce low but non-zero values of rainfall for regions away from the storm, as illustrated in Figure 5.1d and 5.1e, respectively. As the other rainfall algorithms do not exhibit this property, a comparison of rainfall involving all of the methods may be biased by this difference. Hence the idea of minimum rainfall cutoff values was introduced into the analysis, where any value of rainfall rate less than the specified cutoff would be neglected in the calculation of the area-averaged rainfall. This not only allows a more

(A) Method of Smith & Mugnai (1988) , with land contamination



(B) Method of Smith & Mugnai (1988) , with land contribution removed



(C) Method of Spencer *et al* (1989)

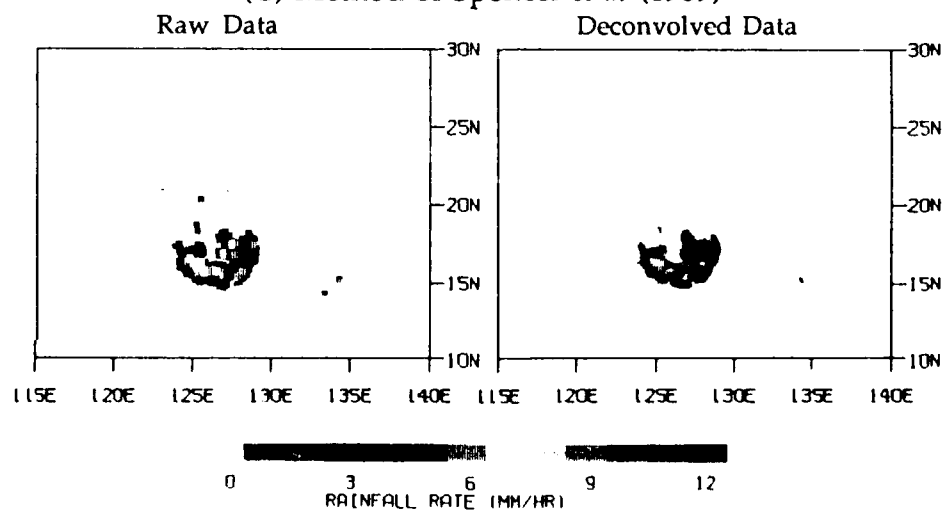
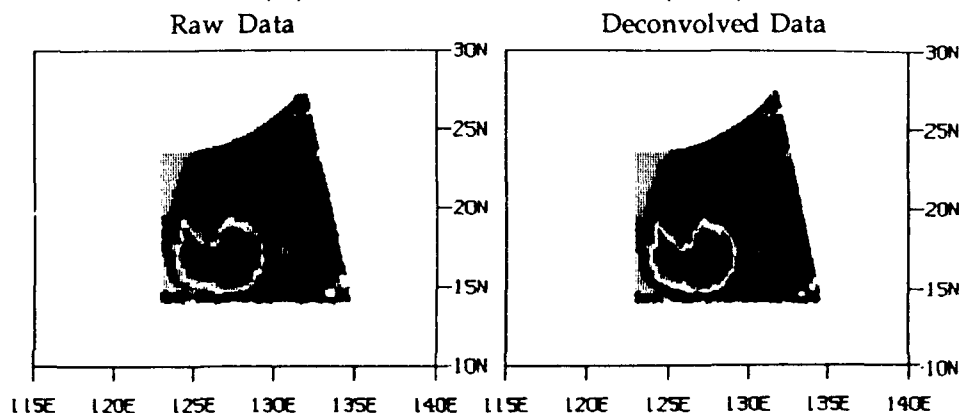


Figure 5.1: Raw/Deconvolved rain rates for various rainfall algorithms

(D) Method of Hinton *et al* (1991)

(E) Method of Olson (1991)

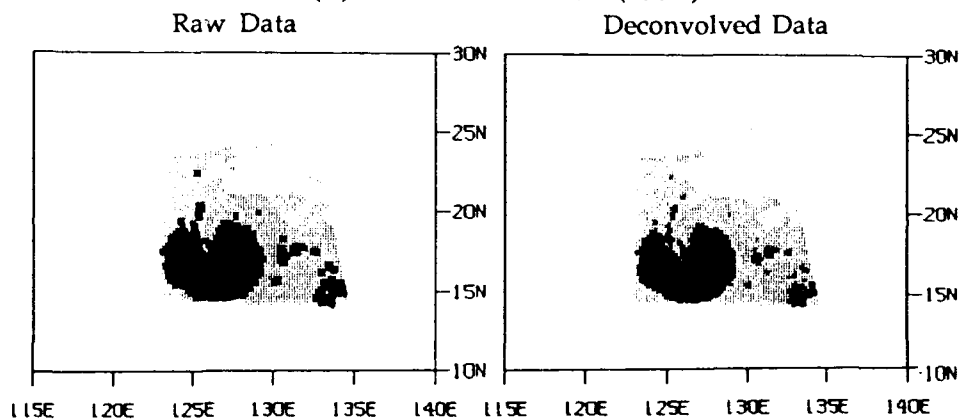
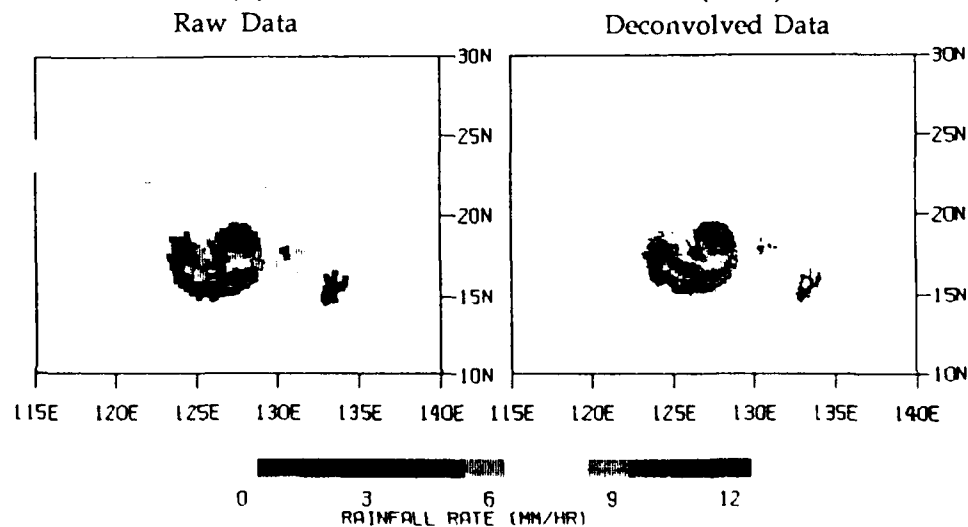
(F) Method of Kummerow *et al* (1991)

Figure 5.1: Continued

thorough comparison between the different methods, but allows the effect of the deconvolution method on more intense rain areas to be isolated.

For the sake of brevity, graphic representations of these area-averaged rainfall time series will be limited to Super Typhoon Thelma. The first such time series, presented in Figure 5.2, is derived from the application of the algorithm of Smith and Mugnai (1988). Figure 5.2a, which presents area-averaged rain rate versus time (derived from raw SSM/I brightness temperatures) for four minimum cutoff rainfall rates, has several interesting features. The rainfall peak on day 193 (on the left of the figure) corresponds well with the time of maximum intensity reported by Hoffman *et al.* (1987), and grows as expected when higher cutoff values are imposed. However, the sharp minimum left of this peak appears lower than it should, as the coverage of that particular overpass missed the eyewall and the contribution of its heavy rainfall. The peak on day 195 (on the right of the figure), which appears at higher cutoff values, is an aberration which occurs due to the small number of pixels which exceed the higher rain rates. Another interesting feature present in Figure 5.2a is the overall behavior of the plots as a function of cutoff rainfall rate. There is a large separation between the plots for the first two cutoffs, that of 0 and 1 mm•hr⁻¹. This is due to the large areas of light rainfall away from the central eyewall (seen in Figure 5.1b) and their contribution to the area average.

The effect of deconvolution on the retrieved rainfall is illustrated in the second half of the figure, where the area averaged rainfall rates retrieved from the deconvolved data exceeded those retrieved from the raw data by an average of 4.1% for a zero cutoff value, which is represented by a positive

difference in Figure 5.2b. This degree of difference is considered significant for rainfall averaged over such a large area, especially when noting that at some individual grid points, differences exceed $6 \text{ mm} \cdot \text{hr}^{-1}$. These increases are expected as the deblurring effect of the deconvolution process both enhances smaller areas of rainfall not detected in the raw data, and secondly increases the brightness temperatures and likewise the retrieved rain rates for certain points [as governed by the non-linear properties of the brightness temperature - rain rate algorithm, explained by Smith and Kidder (1978)].

The next such analysis is conducted for the single frequency (37 GHz) algorithm of Spencer *et al.* (1989) and is presented in Figure 5.3. The same peaks in rainfall (both the actual peak on the left and the false one on the right) appear here in Figure 5.3a as did for the previous method; however the percent difference diagram of Figure 5.3b is quite different. The values of rain rates derived from deconvolved brightness temperatures were consistently in excess of 10% smaller than those derived from raw data. This is not due to the rainfall algorithm, since the relationship between rain rate and PCT is linear, and an energy conserving enhancement should not significantly change the PCT values. This difference instead is due to the way in which the tuning parameters were selected within the deconvolution method itself. Since the exercise of finding the optimum tuning parameter must be conducted independently for each polarized channel, the values of γ utilized were different for each polarization at 37 GHz, as previously listed in Table 3.1. Due to this difference, the effect of the deconvolution procedure was more pronounced for the 37 GHz horizontally polarized channel. Hence the differing applications of the deconvolution procedure introduced a bias to the

polarization differences, which in turn biased the rainfall rates. This illustrates that the consistency of the deconvolution method between polarizations can be important for certain applications, and hence will be included in future development of the method.

One final notable aspect of the method of Spencer *et al.* (1989) is its inability to detect stratiform rain or light rain (i.e., small drops). This is seen in the precipitation pattern illustrated in Figure 5.1c, where only the major convective band and the eyewall are depicted as raining. The surrounding areas of lighter rain [seen in Figure 5.1b by the algorithm of Smith and Mugnai (1988)] have smaller drops and hence the depolarizing effects due to scattering by larger drops is diminished.

The quantitative analysis of the rainfall algorithm of Hinton *et al.* (1991) is presented in Figure 5.4. The time series of area-averaged rain rate is similar to those of the previous methods. However, the distribution of rain has one distinct difference; the method suffers from overprediction of light rainfall. Figure 5.1d illustrates that large spatial regions far from the storm, judged to be rain free by other methods, are depicted as precipitating. This is due to an inadequately low threshold value of brightness temperature defined by the method (see the Appendix). However, the rainfall rate values for the regions in question are quite low, and can easily be ignored by selecting an appropriate cutoff rainfall rate (i.e., $1 \text{ mm} \cdot \text{hr}^{-1}$). Also of note is that the low rainfall rates (below the $1 \text{ mm} \cdot \text{hr}^{-1}$ cutoff) contribute the least variation to the difference between deconvolved and raw rain rates. This is seen in Figure 5.4b by the closeness of the plots for the $0 \text{ mm} \cdot \text{hr}^{-1}$ and $1 \text{ mm} \cdot \text{hr}^{-1}$ cutoff rainfall values.

The most interesting aspect of the method of Hinton *et al.* (1991) is the apparent insensitivity of its area averaged rainfall to the deconvolution process, as seen in Figure 5.4b. This is dominated by the behavior of the 18 GHz algorithms, as these algorithms respond more to larger values of rainfall rate (described in the Appendix), and regions of heavy rainfall tend to dominate the area average. One reason is that these algorithms are simply less sensitive than others. Whereas the difference between rain rates derived from raw and deconvolved brightness temperatures exceeded $6 \text{ mm} \cdot \text{hr}^{-1}$ at individual pixels for the algorithm of Smith and Mugnai (1988), such differences remained less than $2 \text{ mm} \cdot \text{hr}^{-1}$ for these algorithms. However the main reason the area-averaged rain rates changed little was the maximum threshold rainfall rate. The algorithms are devised in such a way so as to set the rainfall rate to $12 \text{ mm} \cdot \text{hr}^{-1}$ if the rate produced exceeds that value (see the Appendix). Notably, that threshold is exceeded for a large portion of each storm. In those places the deconvolved and raw values of rain rates are both equal to the threshold and therefore the deconvolution procedure has no effect. These identical maximum rain areas, when combined with low rain rate areas which have a minimal impact on the area average, produce an average rain rate which is relatively insensitive to the deconvolution process. This may be due to the fact that the radiative model was prescribed with physical parameters consistent with precipitation over the Indian ocean, which did not consider the intense rainfall present in the typhoon cases of this study.

The analysis of the algorithm of Olson (1991) is presented in Figure 5.5. Unlike the others, area averaged rainfall obtained from this algorithm

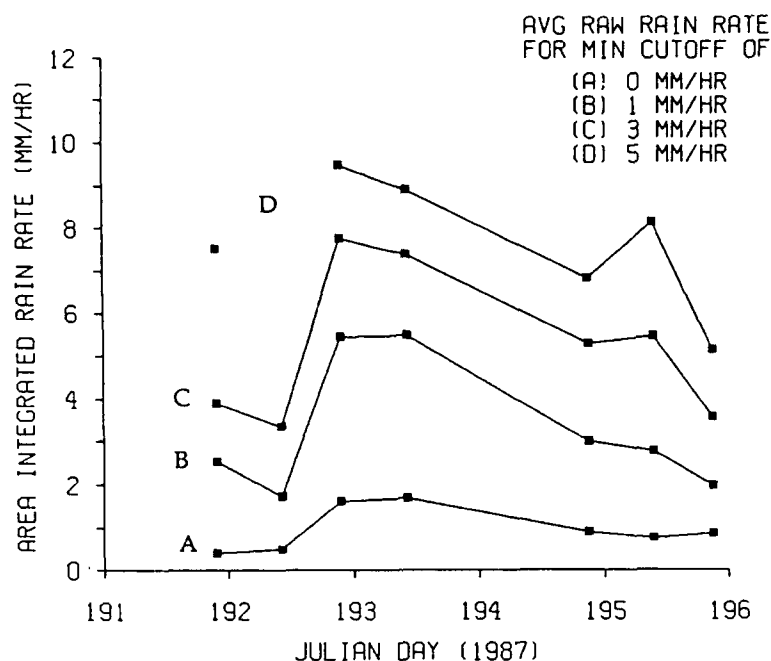
apparently does not respond to changes in storm intensity. While Figure 5.5a shows very little change in area averaged rainfall with time, significant changes in storm intensity were reported [Hoffman *et al.* (1987)] during that same period. This is explained by the fact that this algorithm produces only small values of rainfall rates, which can be seen by comparing the actual values plotted in Figure 5.5a with the corresponding plots of the other methods. This may also be seen in the actual rainfall map (Figure 5.1e), which exhibits very low rainfall rates when compared to the other methods for the intense convective band and eyewall. The author of this algorithm has pointed out to us that this behavior is due to a lack of heavy rainfall cases in the derivation of the regression coefficients. This arises because tropical storms are difficult to comprehensively analyze with radar data, since such storms are not near land during much of their lifetime. The author is currently considering this problem before the algorithm is finalized.

The analysis of the final algorithm, that of Kummerow *et al.* (1991), is presented in Figure 5.6. The time sequence of area-averaged rainfall, depicted in Figure 5.6a, is less sensitive to storm intensity and displays lower rainfall values (see Figure 5.1f) than the first three algorithms discussed. The peak in rainfall near day 193 is weak but still noticeable, unlike the time record for Olson (1991), which appears nearly flat. Also the actual rainfall values displayed in the rainfall map of Figure 5.1f are less than those of the first three algorithms discussed, although twice as large as those of Olson (1991), shown in Figure 5.1e. The effect of deconvolution on the area-averaged rain rate, depicted in Figure 5.6b, is not straightforward. The difference of deconvolved and raw rain rates varies in sign and in magnitude from one scene to the

next, although when averaged over the entire time series, this difference appears small. Individual scenes within the series may have values significantly greater or less than the time mean, such that the small overall time average may be misleading. As described in the Appendix, this algorithm utilizes relationships derived from a series of 25 cloud models. These cloud models employ the effects of many radiative properties, such as emission and scattering, all of which have varied responses to the presence of precipitation with varying degrees of non-linearity. Interpretations are also complicated by the averaging process, since several of the 25 models may be used within a single SSM/I scene and each are sensitive in different ways.

(A) Raw area-averaged rainfall rates

METHOD OF SMITH AND MUGNAI (1988)



(B) Percent difference between deconvolved and raw rain rates

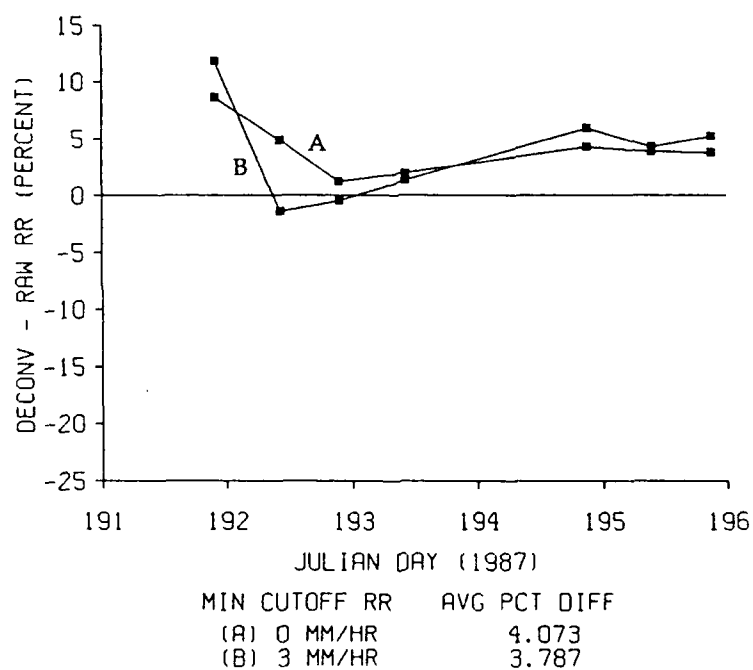
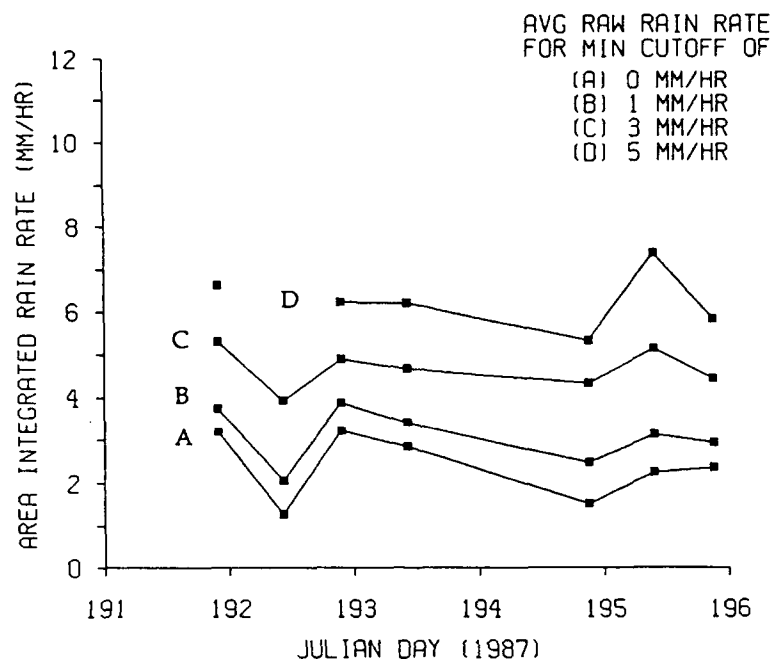


Figure 5.2: Raw area-averaged rain rates and percent differences (between deconvolved and raw rain rates) for the algorithm of Smith & Mugnai (1988).

(A) Raw area-averaged rainfall rates

METHOD OF SPENCER ET AL (1989)



(B) Percent difference between deconvolved and raw rain rates

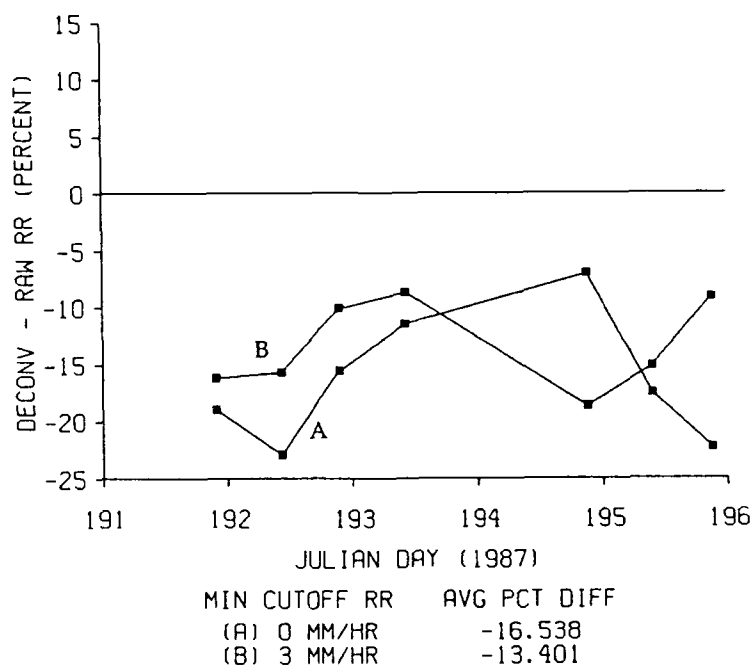
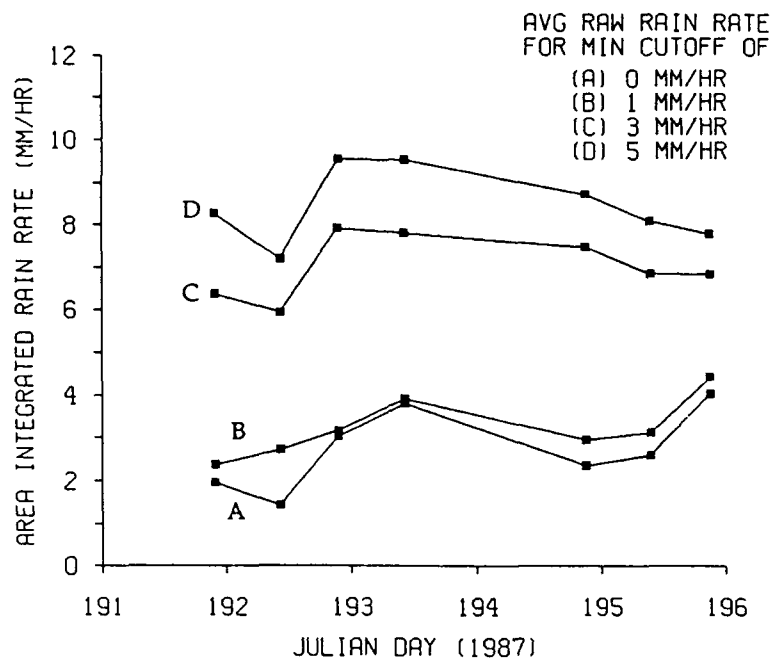


Figure 5.3: Raw area-averaged rain rates and percent differences (between deconvolved and raw rain rates) for the algorithm of Spencer *et al.* (1989).

(A) Raw area-averaged rainfall rates

METHOD OF HINTON ET AL (1991)



(B) Percent difference between deconvolved and raw rain rates

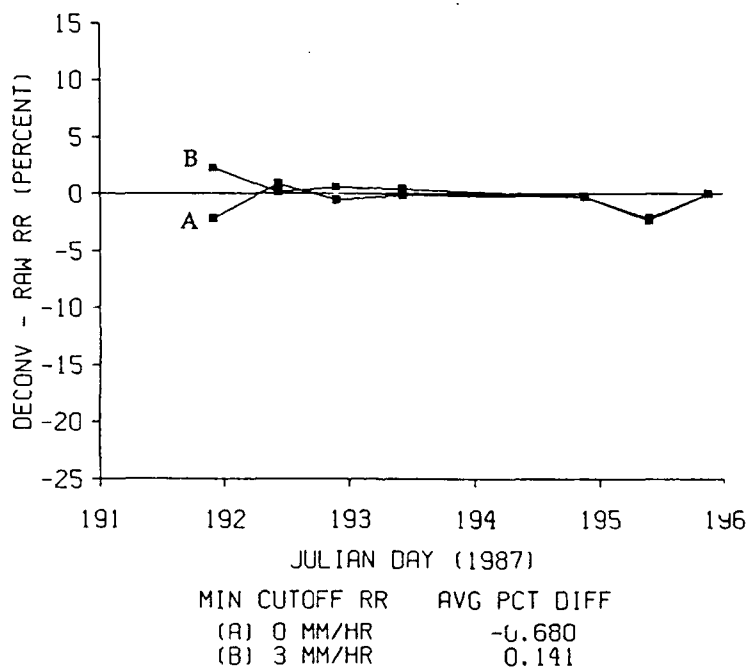
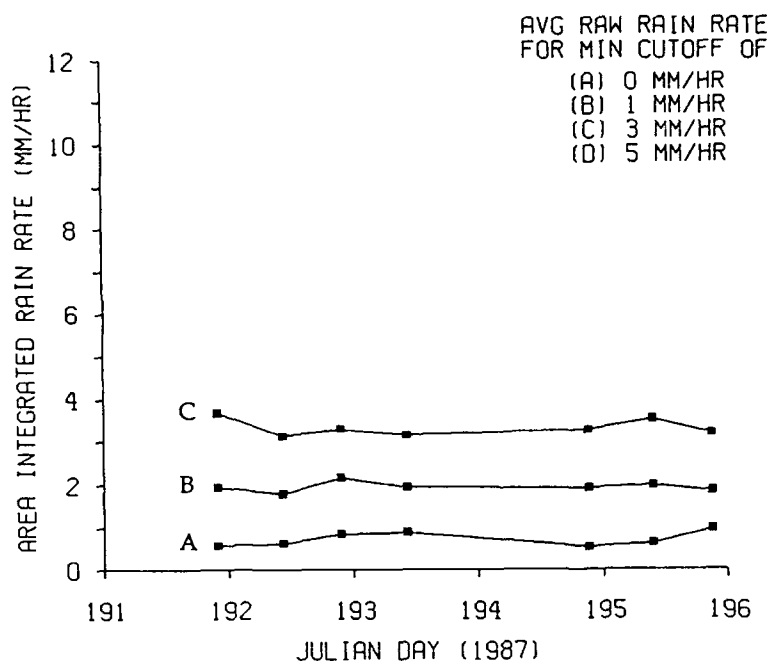


Figure 5.4: Raw area-averaged rain rates and percent differences (between deconvolved and raw rain rates) for the algorithm of Hinton *et al.* (1991).

(A) Raw area-averaged rainfall rates

METHOD OF OLSON (1991)



(B) Percent difference between deconvolved and raw rain rates

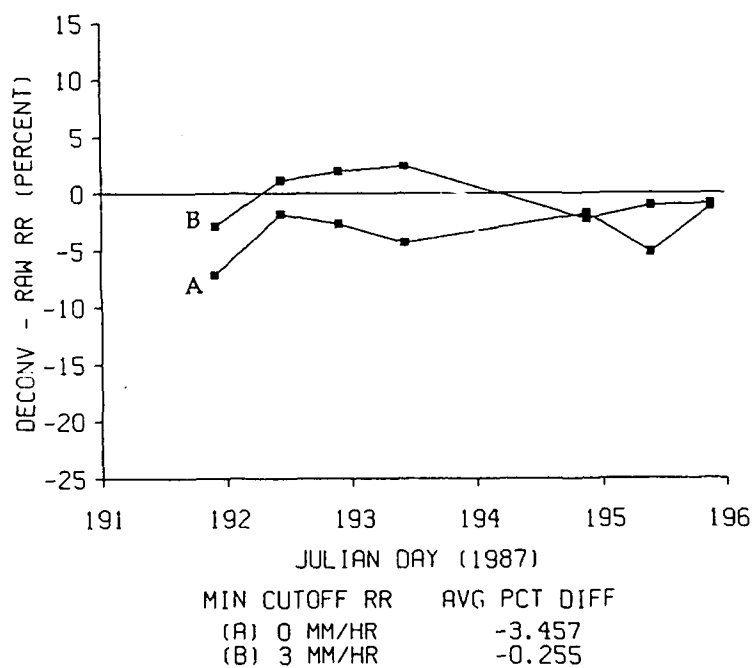
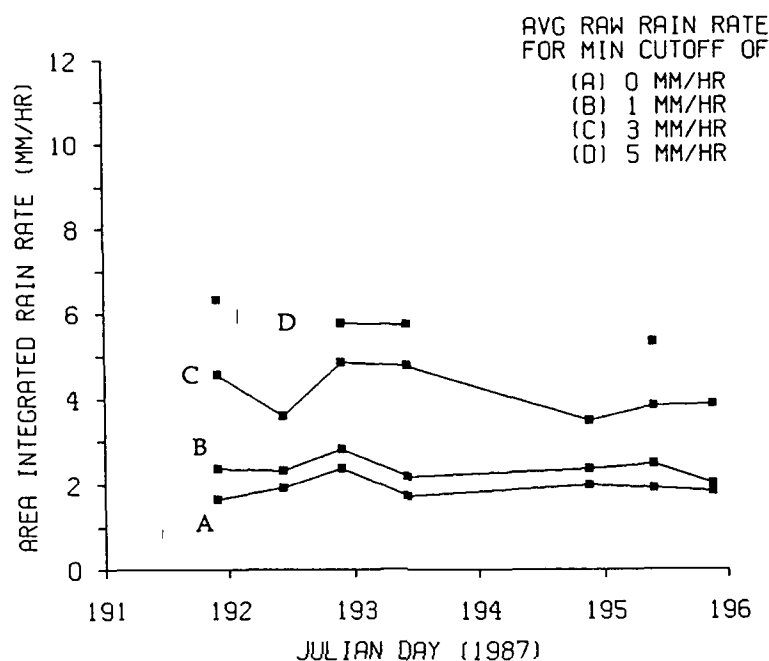


Figure 5.5: Raw area-averaged rain rates and percent differences (between deconvolved and raw rain rates) for the algorithm of Olson (1991).

(A) Raw area-averaged rainfall rates

METHOD OF KUMMEROW ET AL (1991)



(B) Percent difference between deconvolved and raw rain rates

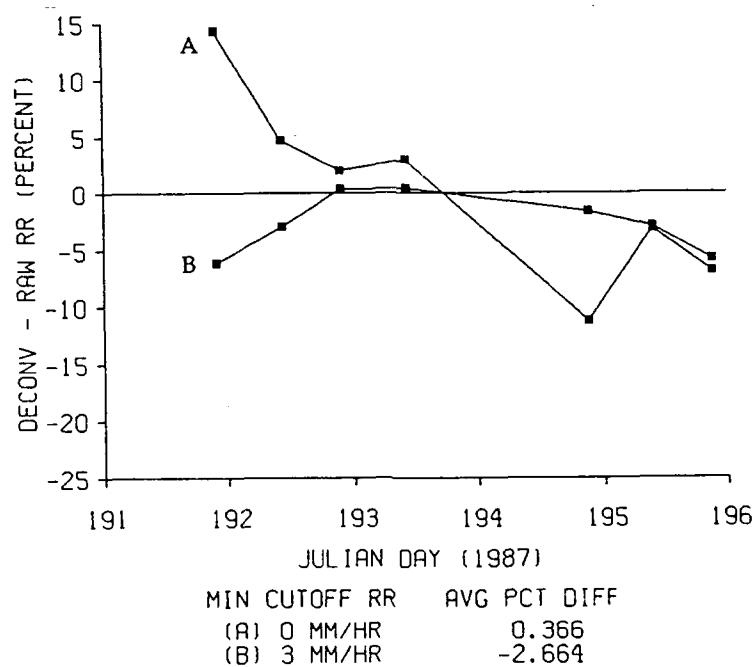


Figure 5.6: Raw area-averaged rain rates and percent differences (between deconvolved and raw rain rates) for the algorithm of Kummerow *et al.* (1991).

CHAPTER 6

Summary and Conclusions

The five rainfall retrieval algorithms were also applied to six additional tropical storm cases. The numerical compilation of the percent differences between deconvolved and raw area-averaged rain rates for all the cases is presented in Table 6.1, with averaged results for all cases appearing in Table 6.2. The same types of patterns detected for Super Typhoon Thelma are also present in the other case studies. The area-averaged rainfall derived from the algorithm of Smith and Mugnai (1988) is increased for every case. Also biases introduced between the two 37 GHz polarized channels by the deconvolution method lead to reductions in area-averaged rainfall for the algorithm of Spencer *et al.* (1989) in every tropical storm case. The area-averaged rainfall from the algorithm of Hinton *et al.* (1991) remains insensitive to the deconvolution process, as illustrated by the small values shown in Tables 6.1 and 6.2. The rainfall from the method of Olson (1991) did not respond to the changes in intensity for the other storm cases and continued to yield the lowest values of rainfall, when compared to the other methods. The most notable example of this was for Hurricane Hillary, where the rainfall values for nearly all pixels was under $1 \text{ mm} \cdot \text{hr}^{-1}$. The tiny number of pixels measuring rain above the $1 \text{ mm} \cdot \text{hr}^{-1}$ cutoff yielded extreme values for the

percent difference between deconvolved and raw rain rates presented in Table 6.1, such that they were not included in the average presented in Table 6.2. The final algorithm, that of Kummerow *et al.* (1991), was run by the author of that algorithm for the case of Super Typhoon Thelma only. Hence the average values presented in Table 6.2 includes data from that one case only.

The effect of deconvolution of lower frequency SSM/I channels has been illustrated by its impact on rainfall rates derived from five different rainfall retrieval algorithms. The independent treatment of different polarized channels introduced a bias in polarized differences, which lead to decreased rainfall from a single channel scattering algorithm. Hence future development and improvements of our deconvolution will address this problem. More favorable results were obtained for a single channel emission algorithm, which will inherently underestimate rainfall due to non-complete beam filling of the large 19 GHz field of view. The deconvolution method improved the resolution of the scene, which lead to increased estimates of rainfall. While the deconvolution process produced smaller impacts on area-averaged rainfall for the other algorithms tested, smaller scale features were enhanced in the rainfall images for all the algorithms, such as was shown for terrestrial features in Chapter 4. This method, by improving the retrieved rainfall and the spatial distribution of rainfall within storms, can make positive contributions to the analysis and forecasting of precipitating systems.

Table 6.1: Percent difference between deconvolved / raw -derived rain rates for each tropical storm case at various minimum cutoff rain values

method	storm	Minimum rainfall rate cutoff values			
		0 mm•hr ⁻¹	1 mm•hr ⁻¹	3 mm•hr ⁻¹	5 mm•hr ⁻¹
A) Smith and Mugnai (1988)	Arlene		6.613 %	6.500 %	19.859 %
	4.440 %				
	Betty	3.789	4.238	5.369	1.956
	Cary	4.201	3.325	4.299	1.743
	Greg	2.363	3.003	5.426	6.027
	Hillary	5.059	6.044	9.776	6.881
	Thelma	4.073	5.358	3.787	5.462
	Wynne	11.613	19.600	5.370	4.762
B) Spencer <i>et al.</i> (1989)	Arlene	-18.237 %	-16.485 %	-10.672 %	-6.063 %
	Betty	-9.338	-7.418	-7.684	-7.327
	Cary	-12.220	-8.982	-8.882	-9.632
	Greg	-27.302	-18.882	-10.068	-11.629
	Hillary	-14.843	-10.859	-13.319	-9.573
	Thelma	-16.539	-14.850	-13.401	-11.214
	Wynne	-15.794	-13.993	-11.142	-10.361
C) Hinton <i>et al.</i> (1991)	Arlene	-0.556 %	-1.338 %	-0.651 %	0.485 %
	Betty	-0.664	-0.837	-0.670	0.422
	Cary	-0.745	-0.785	-0.853	0.852
	Greg	-0.342	-0.897	-0.953	0.102
	Hillary	-0.767	-1.032	-0.908	0.291
	Thelma	-0.680	-0.566	0.141	0.387
	Wynne	-0.638	-0.829	-0.444	0.821
D) Olson (1991)	Arlene	-3.571 %	-3.608 %	-0.991 %	N/A
	Betty	-4.359	-2.190	1.164	0.831
	Cary	-2.462	-1.723	1.080	0.301
	Greg	-1.581	-1.198	-0.603	N/A
	Hillary	-0.131	22.623	42.755	150.073
	Thelma	-3.457	-1.760	-0.255	N/A
	Wynne	-3.464	-4.127	-1.502	-3.585
E) Kummerow <i>et al.</i> (1991)	Thelma	0.366 %	-0.320 %	-2.664 %	-1.318 %

Table 6.2: Average percent difference between deconvolved / raw -derived rain rates for various minimum cutoff rain values

<u>method</u>	<u>0 mm•hr⁻¹</u>	<u>1 mm•hr⁻¹</u>	<u>3 mm•hr⁻¹</u>	<u>5 mm•hr⁻¹</u>
Smith and Mugnai (1988)	5.753 %	7.429 %	7.685 %	4.279 %
Spencer <i>et al.</i> (1989)	-15.567	-12.611	-10.675	-9.291
Hinton <i>et al.</i> (1991)	-0.646	-0.897	-0.617	0.527
Olson (1991)*	-2.783	-2.567	-0.159	-0.935
Kummerow <i>et al.</i> (1991) **	0.366	-0.320	-2.664	-1.318

* - Average neglects values from Hurricane Hillary (as given in Table 3)

** - Values consist only of data from ST Thelma

APPENDIX

Rainfall Retrieval Algorithms

A.1 Smith and Mugnai (1988)

This single frequency (19 GHz) rainfall algorithm was developed from simulations of a microwave radiative transfer model of precipitating clouds. This model [developed by Mugnai and Smith (1988)] coupled a highly detailed solution of the radiative transfer equation to an explicit microphysical model of a time dependent cumulus cloud. The simulation studies of the model produced rainfall rates at the model frequencies as a function of upwelling brightness temperature at the top of the atmosphere (TOA), cloud development time (characteristic of the state of the developing cloud) and thickness of the rain layer. Knowledge of rainfall rates as a function of the microphysical and dynamical aspects of a precipitating cloud was incorporated within the model framework, such that a most probable rainfall rate was associated with each cloud development time. Hence a most probable rain rate for particular values of rain layer thickness as a function of TOA brightness temperature was developed.

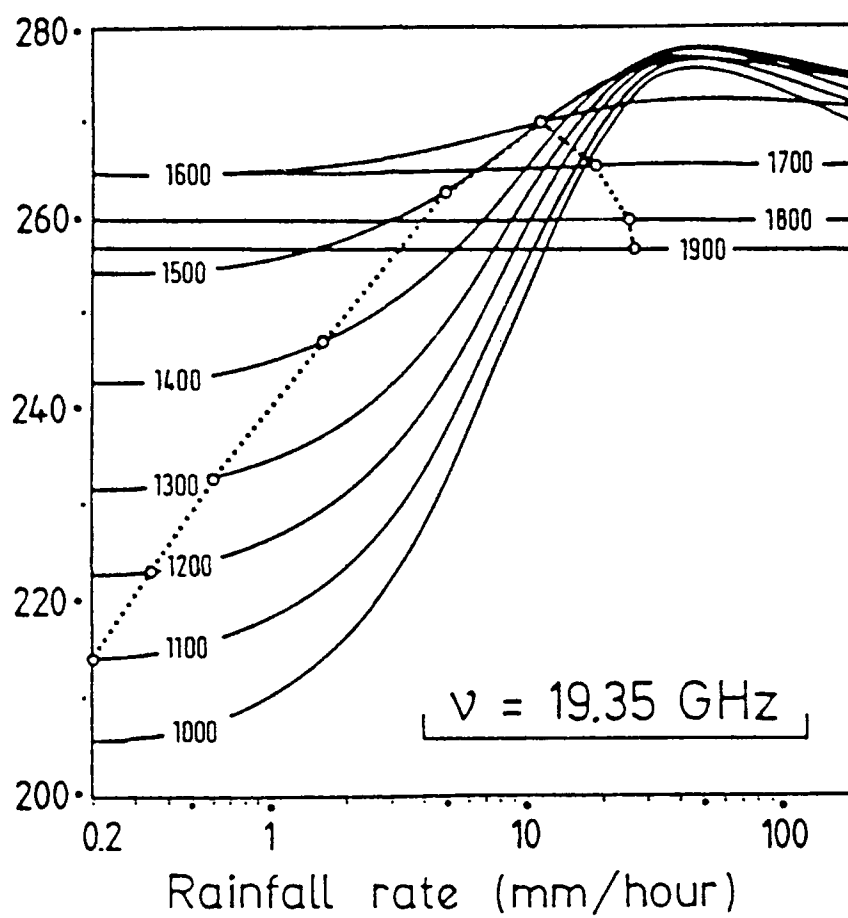


Figure A.1: Area integrated rainfall rate as a function of time. Results for the raw data are shown with the narrow black line; results for the deconvolved data are shown with the wide gray line.

This functional relationship for 19 GHz is presented in Figure A1. The most notable feature of this diagram is its double valued nature. As the cloud develops, absorption of the underlying rain signal by the cloud media grows rapidly and the cloud layer itself begins to provide most of the signal detected at TOA. As the cloud continues to develop and achieve higher rainfall rates, its optical depth reaches a critical limit in which scattering in the upper cloud plays an important role in masking radiation from the lower cloud. Hence the rainfall rate as a function of TOA brightness temperature appears as a double valued function.

A.2 Spencer *et al.* (1989)

This single frequency (37 GHz) algorithm is based on the depolarization of microwave brightness temperatures due to the scattering by hydrometeors, which was shown to be dominated by the effects of ice. As these hydrometeors (especially ice) scatter radiation signals out of the path, the values of the resulting satellite measured brightness temperatures are reduced. It was then shown that the polarization diversity of the SSM/I measurements allowed low brightness temperatures due to the ocean surface to be distinguished from those due to scattering from precipitation.

Such polarization information was represented in terms of a polarization corrected temperature (PCT), defined as:

$$PCT = (\beta T_{Bh} - T_{Bv}) / (\beta - 1) \quad (A.1)$$

$$\text{where} \quad \beta = (T_{Bvc} - T_{Bvo}) / (T_{Bhc} - T_{Bho}) \quad (\text{A.2})$$

Here T_{Bvc} and T_{Bhc} refer to the respective polarized T_B 's over a cloud free ocean, while T_{Bvo} and T_{Bho} are the T_B 's over the ocean with no overlying atmosphere. Each of these parameters were derived from model calculations for a standard tropical atmosphere over the ocean at the SSM/I viewing angle of 53° . As actual SSM/I measurements differed significantly from the model results, an empirically modified value of β was used. When this value was applied to the 37 GHz measurements, the expression for the polarization corrected temperature at 37 GHz reduced to the following:

$$PCT_{37} = 2.1 T_B(37V) - 1.1 T_B(37H) \quad (\text{A.3})$$

A threshold value of the PCT was then derived such that any value larger than the threshold would be considered too highly polarized to represent significant precipitation. As this method relies on effects due to ice and large hydrometeors, it fails to identify shallow, light precipitation. Finally rainfall rates were then inferred from the threshold PCT (270 K) and the 37 GHz polarization corrected temperatures by

$$\text{Rainfall Rate (mm}\cdot\text{hr}^{-1}) = 270 - PCT_{37} \quad (\text{A.4})$$

A.3 Hinton *et al.* (1991)

This algorithm is a series of single channel hybrid physical/statistical models developed for the SMMR (Scanning Multichannel Microwave Radiometer) instrument aboard the Nimbus 7, and is explained in detail by Martin *et al.* (1990). A plane-parallel, 120 layer radiative transfer model was used to determine the upwelling brightness temperatures over a 1° by 1° latitude box as a function of many model parameters, most of which were prescribed with typical climatological values or values obtained from statistical model tests. Sensitivity tests of all these parameters found that variations in non-precipitating cloud liquid water content (LWC) dominated the variations in the resultant brightness temperatures. The presence of non-precipitating cloud liquid water not only introduces uncertainty in the rate of precipitation obtained from such a model, but also has been linked to the dynamical processes which produce precipitation. A semi-empirical relationship between rainfall rate and non-precipitating LWC was introduced in an effort to remove some ambiguity in a model-derived relationship between rain rate and brightness temperature. The results for each 1° by 1° box were then integrated with a prescribed statistical distribution to match the field of view of the SMMR instrument, so that an area averaged rainfall rate could be calculated from an area averaged brightness temperature measured by the instrument.

The following equations result from a polynomial regression of the average rainfall rate against the average brightness temperature for each single channel model.

$$\begin{array}{ll}
 0 & T_B(18V) \leq 192.283 \\
 RR_{18V} = 0.06295 [T_B(18V) - 192.283] & , \text{ for } T_B(18V) > 192.283 \quad (A.5a) \\
 + 2.0 \cdot 10^{-5} [T_B(18V) - 192.283]^3 &
 \end{array}$$

$$12 \quad RR_{18V} > 12$$

$$\begin{array}{ll}
 0 & T_B(18H) \leq 133.763 \\
 RR_{18H} = 0.038162 [T_B(18H) - 133.763] & , \text{ for } T_B(18H) > 133.763 \quad (A.5b) \\
 + 3.87 \cdot 10^{-6} [T_B(18H) - 133.763]^3 &
 \end{array}$$

$$12 \quad RR_{18H} > 12$$

$$\begin{array}{ll}
 0 & T_B(37V) \leq 213.38 \\
 RR_{37V} = -5.0199 + 0.02333 T_B(37V) + & , \text{ for } T_B(37V) > 213.38 \quad (A.5c) \\
 0.6272 \cdot \exp \{ [T_B(37V) - 258]/3.3655 \} &
 \end{array}$$

$$12 \quad RR_{37V} > 12$$

$$\begin{array}{ll}
 0 & T_B(37H) \leq 159.42 \\
 RR_{37H} = -1.3973 + 0.008942 T_B(37H) + & , \text{ for } T_B(37H) > 159.42 \quad (A.5d) \\
 3.8394 \cdot \exp \{ [T_B(37H) - 258]/11.0530 \} &
 \end{array}$$

$$12 \quad RR_{37H} > 12$$

These four algorithms were weighed by the inverses of their variances, which were determined experimentally from model studies of each channel. As the measurement errors are assumed to be random, it follows that the individual weights are proportional to the inverse square of the derivative of RR with respect to T_B times the error variance, for each channel. The weights for each channel can then be expressed as a function of its respective rainfall rate, as follows:

$$\begin{aligned}
 W_{18V} &= 0.175 \cdot [1 - \exp(-1.53 \text{ RR}_{18V})] \cdot \exp(0.0717 \text{ RR}_{18V}) \\
 W_{18H} &= 0.516 \cdot [1 - \exp(-1.39 \text{ RR}_{18H})] \cdot \exp(-0.0698 \text{ RR}_{18H}) \\
 W_{37V} &= 0.004 + 0.125 \cdot \exp(-\text{RR}_{37V}) \\
 W_{37H} &= 0.019 + 0.776 \cdot \exp(-\text{RR}_{37H})
 \end{aligned} \tag{A.6}$$

The total rainfall is then found by applying the weights of equation (A.6) to each respective single channel rainfall found from equation (A.7), and then dividing by the sum of the weights. Finally, of note is that while the regression equations were developed for the SMMR frequencies of 18 and 37 GHz, they were used with SSM/I data measured at 19 and 37 GHz.

A.4 Olson (1991)

This multiple frequency algorithm begins with two physical quantities retrieved with the SSM/I measurements. The first is near-surface wind speed (U) over the ocean, given by Goodberlet *et al.* (1989) as a function of brightness temperature at 19, 22 and 37 GHz. The second quantity is the total precipitable

water (V), given by Petty and Katsaros (1990) as a function of brightness temperature at 19 and 22 GHz. These physical quantities are utilized to calculate normalized polarization differences at 85 and 37 GHz:

$$P37 = [T_B(37V) - T_B(37H)] \cdot \exp (0.0151 U + 0.00607 V - 4.40) \quad (A.7)$$

and

$$P85 = [T_B(85V) - T_B(85H)] \cdot \exp (0.0241 U + 0.0271 V - 4.44) \quad (A.8)$$

A scattering depression at 85 GHz (S85) is then defined in terms of P85 by

$$S85 = P85 \cdot TB_{85V_0} + 273 (1-P85) - TB_{85V} \quad (A.9)$$

where

$$TB_{85V_0} = 280.0 - \exp (4.20 - 0.00567 U - 0.0406 V) \quad (A.10)$$

Olson (1991) then performed a statistical regression between two of these quantities (S85 and P37) to radar-retrieved rainfall rates. The resultant regression formula is given as

$$RR \text{ (mm} \cdot \text{hr}^{-1}) = \exp (2.24395 + 0.00358838 \cdot S85 - 0.169310 \cdot P37) - 8.0 - \text{Bias (latitude)} \quad (A.11)$$

where the bias correction (based on retrieval histograms performed for January and July, 1988) does not exceed 0.2 mm•hr⁻¹.

At the time this article was prepared, the preceding was still a trial algorithm and its development was ongoing. Among other improvements,

the author was attempting to eliminate the bias correction by reformulating the predictors S85 and P37.

A.5 Kummerow *et al.* (1991)

This multiple frequency algorithm employs relationships between rain rates and brightness temperatures, derived from a set of 25 cloud radiative models. Each model consists of five vertical layers and specifies a distinct vertical cloud structure in terms of cloud liquid water and rain rate. Ten of the models are defined as "convective," indicating the presence of significant quantities of liquid and frozen hydrometeors above the freezing level. Ten models are identified as "stratiform," indicating the absence of liquid hydrometeors above the freezing level. The final five models are defined as "anvil clouds," characterized by ice aloft but no significant precipitation at the surface, such as those often observed in downwind or "blowoff" regions of convective systems. The retrieval scheme determines which of these models best represents the observed meteorological conditions as outlined by the following procedure.

First, various quantities within each cloud model are varied randomly to produce a large set of possible clouds. Multiple linear regression techniques are applied to the upwelling brightness temperatures produced by the model to obtain regression coefficients relating the rainfall rate (RR) to a linear combination of the observed brightness temperatures. This is expressed by

$$RR \text{ (mm/hr)} = a_0 + \sum_{i=1}^N a_i T_{B_i} \quad (\text{A.11})$$

where N is the total number of channels (7 for SSM/I), T_{B_i} is the brightness temperature for each respective channel, and a_0 and a_i are the regression coefficients. In requiring consistency between the observed TB's those calculated from the models, the retrieval scheme determines which of these models best represents the observed meteorological conditions.

References

- Backus, G., and F. Gilbert, 1970: Uniqueness in the inversion of inaccurate gross earth data. *Phil. Trans. Roy. Soc. London*, **A266**, 123 - 192.
- Case, R.A. and H.P. Gerrish, 1988: Annual summary: Atlantic hurricane season of 1987. *Monthly Weather Rev.*, **116**, 939-949.
- Claassen, J.P. and A.K. Fung, 1974: The recovery of polarized apparent temperature distributions of flat scenes from antenna temperature measurements. *IEEE Trans. Ant. Prop.*, **AP-22**, 433-442.
- Cross, R.L., 1988: Annual summary: eastern north Pacific tropical cyclones of 1987. *Monthly Weather Rev.*, **116**, 2106-2117.
- Hinton, B.B., W.S. Olson, D.W. Martin and B. Auvine, 1991: A passive microwave algorithm for tropical oceanic rainfall. Submitted to *J. Appl. Meteor.*
- Hoffman, C.W., V.G. Patterson and D.J. McMorrow, 1987: 1987 Tropical cyclone report. Joint Typhoon Warning Center, Guam, 213 pp.
- Hollinger, J., 1989: DMSP Special Sensor Microwave/Imager calibration/validation. Final Report, Volume 1, Naval Research Laboratory, Washington, D.C.
- Holmes, J.J., C.A. Balanis and W.M. Truman, 1975: Application of Fourier transforms for microwave radiometric inversions. *IEEE Trans. Ant. Prop.*, **AP-23**, 797-806.
- Kummerow, C., I.M. Hakkarinen, H.F. Pierce and J.A. Weinman, 1991: Determination of precipitation profiles from airborne passive microwave radiometric measurements. *J. Atm. Oceanic Tech.*, **8**, 148 - 158.
- Lewis, B.M. and D.P. Jorgensen, 1978: Study of the dissipation of Hurricane Gertrude (1974). *Monthly Weather Rev.*, **106**, 1288-1306.

- Martin, D.W., B.B. Hinton, B. Auvine and W.S. Olson, 1990: Use of microwave satellite data to study variations in rainfall over the Indian Ocean. Final Report on Grant NAGW-920, Space Science and Engineering Center, University of Wisconsin, Madison, WI, pp. 58.
- Mugnai, A. and E.A. Smith, 1988: Radiative transfer to space through a precipitating cloud at multiple microwave frequencies. Part I: Model description. *J. Clim. Appl. Meteor.*, **27**, 1055 - 1073..
- Olson, W.S., 1991: The use of WetNet as a tool for precipitation algorithm intercomparisons, browse algorithms, and PC library of algorithms for recalculation, validation, and algorithm integration. Presented at WetNet Science and Analysis Colloquium, UCSB, Santa Barbara, CA, 19-22 February 1987.
- Petty, G.W. and K.B. Katsaros, 1990: New geophysical algorithms for the Special Sensor Microwave Instrument. Preprints, 5th Conference on Satellite Meteor. and Oceanography (AMS), London, England, 247-251.
- Poe, G., 1990: Optimum interpolation of imaging microwave radiometer data. *IEEE Trans. on Geosci. and Remote Sens.*, **GE-28**, 800 - 810.
- Rodgers, E.B. and R.F. Adler, 1981: Tropical cyclone rainfall characteristics as determined from a satellite passive microwave radiometer. *Monthly Weather Rev.*, **109**, 506-521.
- Smith, E.A., and S.Q. Kidder, 1978: A multispectral satellite approach to rainfall estimates. Presented at the 18th AMS Conference on Radar Meteorology, Atlanta, GA, 28-31 March 1978.
- Smith, E.A., and A. Mugnai, 1988: Radiative transfer to space through a precipitating cloud at multiple microwave frequencies. Part II: Results and analysis. *J. Appl. Meteor.*, **27**, 1074 - 1091.
- Spencer, R.W., H.M. Goodman and R. Hood, 1989: Precipitation retrieval over land and ocean with the SSM/I: identification and characteristics of the scattering signal. *J. Atm. Oceanic Tech.*, **6**, 254 - 273.
- Spencer, R.W., 1986: A satellite passive 37 GHz scattering-based method for measuring oceanic rain rates. *J. Clim. Appl. Meteor.*, **25**, 754 - 766.
- Stogryn, A., 1978: Estimates of brightness temperatures from scanning radiometer data. *IEEE Trans. on Ant. and Prop.*, **AP-26**, 720 - 726.

Wilheit, T.T., A.T.C. Chang, M.S.V. Rao, E.B. Rodgers and J.S. Theon, 1977: A satellite technique for quantitatively mapping rainfall rates over the ocean. *J. Appl. Meteor.*, 16, 551 - 560.

Biographical Sketch

Michael Farrar was born in Nashville, TN on June 24, 1964. He graduated from Purdue University in May, 1986 with a B.S. in physics, at which time he was also commissioned as a 2Lt in the U.S. Air Force. He then went to Penn State University, where he received a B.S. in Meteorology in May, 1987. He was then assigned to Headquarters, US Air Forces Europe (USAFE), Ramstein AB, Germany, where he served as a forecaster and command briefer until July, 1989.

Upon his return to the U.S., Michael Farrar then enrolled at Florida State University in order to pursue a Master's degree in Meteorology under Dr. Eric Smith, his major professor. In addition to this thesis, he also presented a paper at the 19th AMS Conference on Hurricanes and Tropical Meteorology in Miami, FL during May 1991. He co-authored (with Dr. Smith) a journal article submitted for publication in the *IEEE Transactions on Geoscience and Remote Sensing*, and plans to submit a second article for publication in the *Journal of Applied Meteorology*, both of which concern the work accomplished in this thesis.

Michael Farrar currently holds the rank of Captain, and will serve at the Scientific Services Division of the Directorate of Weather at SAC Headquarters, Offutt AFB, NE, following his graduation in August, 1991.